Connecting Flow over Complex Terrain to Hydrodynamic Roughness on a Coral Reef

JUSTIN S. ROGERS AND SAMANTHA A. MATICKA

Environmental Fluid Mechanics Laboratory, Department of Civil and Environmental Engineering, Stanford University, Stanford, California

VED CHIRAYATH

NASA Ames Laboratory for Advanced Sensing, Moffett Field, California

C. BROCK WOODSON

College of Engineering, University of Georgia, Athens, Georgia

JUAN J. ALONSO

Department of Aeronautics and Astronautics, Stanford University, Stanford, California

STEPHEN G. MONISMITH

Environmental Fluid Mechanics Laboratory, Department of Civil and Environmental Engineering, Stanford University, Stanford, California

(Manuscript received 26 January 2018, in final form 22 May 2018)

ABSTRACT

Flow over complex terrain causes stress on the bottom leading to drag, turbulence, and formation of a boundary layer. But despite the importance of the hydrodynamic roughness scale z_0 in predicting flows and mixing, little is known about its connection to complex terrain. To address this gap, we conducted extensive field observations of flows and finescale measurements of bathymetry using fluid-lensing techniques over a shallow coral reef on Ofu, American Samoa. We developed a validated centimeter-scale nonhydrostatic hydrodynamic model of the reef, and the results for drag compare well with the observations. The total drag is caused by pressure differences creating form drag and is only a function of relative depth and spatially averaged streamwise slope, consistent with scaling for k–δ-type roughness, where k is the roughness height and δ is the boundary layer thickness. We approximate the complex reef surface as a superposition of wavy bedforms and present a simple method for predicting z_0 from the spatial root-mean-square of depth and streamwise slope of the bathymetric surface and a linear coefficient a_1, similar to results from other studies on wavy bedforms. While the local velocity profiles vary widely, the horizontal average is consistent with a log-layer approximation. The model grid resolution required to accurately compute the form drag is O(10–50) times the dominant horizontal hydrodynamic scale, which is determined by a peak in the spectra of the streamwise slope. The approach taken in this study is likely applicable to other complex terrains and could be explored for other settings.

1. Introduction

Flows over complex terrain create variable stresses on the boundary and the nonlinear generation of turbulence that can occur at multiple temporal and spatial scales. For example, flow within coral reef systems is complex because they have irregular, branching morphologies with reef topography varying at scales ranging from centimeters to kilometers (Rosman and Hench 2011). In shallow nearshore regions with rough surfaces such as reefs or rocky shorelines, bottom stress is often a significant term in the momentum balance and the primary form of dissipation loss. Thus, correct

Supplemental information related to this paper is available at the Journals Online website: https://doi.org/10.1175/JPO-D-18-0013.s1.

Corresponding author: Justin Rogers, jsrogers@stanford.edu

DOI: 10.1175/JPO-D-18-0013.1

parameterization of the bottom stress is essential to understanding these flows (Monismith 2007). Bottom stress is typically represented using a bottom drag coefficient C_D. The bulk (or total) bottom drag $C_{D,B}$ is a combination of two components, skin friction drag $C_{D,\tau}$ resulting from tangential stresses and pressure form drag $C_{D,p}$ resulting from nonuniform pressure distribution on the boundary (Kundu and Cohen 2008).

Stresses on the bottom lead to the nonlinear generation of turbulence, which is ubiquitous in flows with high Reynolds numbers (Re). Turbulence causes not only mixing of tracers of environmental interest but also mixing of momentum and the formation of a boundary layer. For a well-developed turbulent boundary layer, an inertial sublayer region exists where mean velocities exhibit a logarithmic profile. Within this region, the mean velocity profile is related to the generation of turbulence by shear at the bed; the boundary layer follows the classical law of the wall, and roughness is often expressed as a hydrodynamic roughness scale z_0 (e.g., Reidenbach et al. 2006; Kundu and Cohen 2008). However, on surfaces where the roughness elements take up a significant fraction of the water column, such as shallow coral reefs, it is unclear if these assumptions hold in these conditions (Lentz et al. 2017).

For flow over complex surfaces, at least three distinct types of roughness configurations exist, each with their own scaling law (Wooding et al. 1973). The first, k-type roughness (where k is a roughness height), is typical of sand grain roughness studies (Nikuradse 1933), where the horizontal spacing is typically somewhat greater than the element height. In this regime, unstable eddies form behind roughness elements that are shed into the flow above the boundary, resulting in a turbulent structure scaled to the height of the roughness elements (Grant and Madsen 1982; Perry et al. 1969; Jimenez 2004). The second type, δ-type roughness (where δ is the boundary layer thickness), results in the formation of stable eddies between roughness elements, which are typically spaced closer than their height. This causes "skimming flow" along the top of the roughness elements, and its turbulent structure is nearly independent of the roughness height (Wooding et al. 1973; Perry et al. 1969; Jimenez 2004). A third class, k–δ-type roughness, is characterized by the formation of eddies in the lee of the roughness elements and the reattachment of flow behind the elements, which requires a relatively small concentration of elements (Wooding et al. 1973). This type of roughness scales with both the height of the roughness elements, and their concentration is defined as the ratio of the frontal area of each element to the average horizontal surface area (Grant and Madsen 1982). Flow over wavy surfaces such as sand bed ripples, as well as over many coral reef forms (as will be demonstrated in the results), is of the k–δ type.

In circulation models, turbulence is often parameterized in Reynolds-averaged Navier–Stokes (RANS) approaches, which require a parameterization of the bottom roughness. New field-scale technology to measure bottom bathymetry is advancing rapidly with increasing resolution, including sonar, hyperspectral, lidar, and fluid-lensing techniques. Measured variability in bathymetry is now often available at scales much smaller than the resolution of the computational grid. Typically, the mean depth value is taken to represent depth in the grid cell, and the remainder of the data is not used.

Significant work has been conducted to measure site-specific hydrodynamic roughness values on reefs (Rosman and Hench 2011; Reidenbach et al. 2006; Rogers et al. 2017, 2016, 2015; Lentz et al. 2016; Hearn 1999; Symonds et al. 1995; Lowe et al. 2005; McDonald et al. 2006; Thomas and Atkinson 1997; Falter et al. 2004), but a clear connection to the reef surface complexity is lacking. Several studies have suggested characterizing a reef surface based on fractal dimension (Hearn 2011a,b), or spectral energy of rugosity (Nunes and Pawlak 2008; Jaramillo and Pawlak 2011), but they lack a connection to measured hydrodynamic roughness. Thus, the state of current practice for computing bottom stress is to estimate a hydrodynamic roughness value based on general site parameters, based on literature from similar systems, or calibrated from field measurements. To our knowledge, there is yet no unified theory for how turbulent flow over complex terrain connects to hydrodynamic roughness or how multiple spatial terrain scales interact to create the total drag.

The aim of this paper is to address the fundamental question of how complex terrain is related to the hydrodynamic roughness, including what horizontal and vertical length scales are important. To address this question, we conducted an extensive field campaign to measure flow on a coral reef and developed a nonhydrostatic hydrodynamic model of the reef based on detailed bathymetric measurements using fluid-lensing techniques (section 2). The field observations are used to compute the spatially varying drag coefficients (section 3). Based on the validated model, we present a simple model to predict total drag on complex terrain using statistics of the surface (section 4). We conclude with an overview discussion (section 5) and summary (section 6).

2. Methods

a. *Hydrodynamic measurements and data analysis*

Ofu Island, American Samoa, lies in the southwest Pacific Ocean (14.2°S, 169.7°W) (Fig. 1a). Because of the

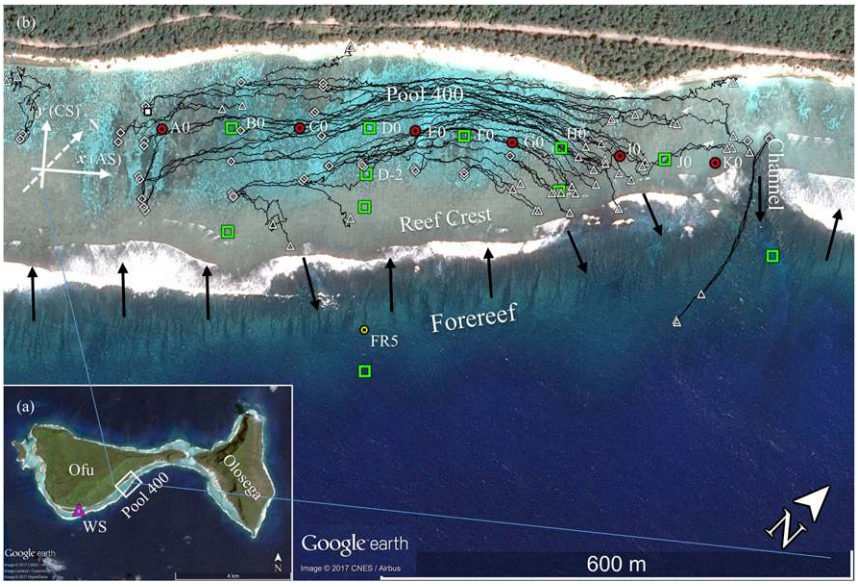

FIG. 1. Field experiment overview, Ofu Reef, American Samoa. (a) Ofu and Olosega Islands, location of pool 400 experiment, and weather station (WS), and (b) pool 400 experiment instrumentation layout showing drifter tracks from subset of drifter releases (black lines) with start (◇) and finish (Δ) and approximate wave-driven flow direction over reef crest (black arrows). Local coordinates of AS and CS directions. Green squares denote velocity, pressure, and temperature measurements, red circles denote high-resolution pressure and temperature measurements, and yellow circles denote low-resolution pressure and temperature measurements (not all shown). Map data: Google Earth, CNES/Airbus.

tidal range and shallow reef crest, the onshore wave-driven flow is forced by breaking waves and modulated by the tides (Koweek et al. 2015). The focus of this study is on pool 400 located on the south shore of Ofu Island within the National Park of American Samoa (Fig. 1b).

The field experiment consisted of an array of velocity, pressure, and temperature sensors deployed from 10 to 28 March 2017 designed to characterize the waves and hydrodynamics of pool 400 (Fig. 1b; appendix). Measurements of velocity data are taken in east, north, and up coordinates and transformed to a local coordinate system with x and y in the alongshore (AS) and cross-shore (CS) directions and z upward from mean sea level (MSL) (Table 1). The instantaneous measurements are time averaged (15 min) to give Eulerian velocity $\mathbf{u}_E(u_E, v_E, w_E)$, free surface deviation from MSL η, and wave statistics. Because of very small waves in pool 400 (Stokes drift $\ll \mathbf{u}_E$), we assume the mean Lagrangian velocity $\mathbf{u} = \mathbf{u}_E$. The Lagrangian depth-averaged mean velocity $\mathbf{U}(U, V, W)$ is calculated by combining data at a given location assuming $\mathbf{u}_E = 0$ at the bottom and averaging over the depth. Additional details are in the appendix.

b. Bathymetric UAV measurements

An airborne survey was conducted over pool 400 in July 2016 using unmanned aerial vehicles (UAV) and fluid-lensing computational methods (Chirayath and Earle 2016; Suosaari et al. 2016; Chirayath 2016) to resolve centimeter-scale bathymetry of the reef (Fig. S1 in the supplemental material). A UAV electric quadcopter platform was custom built to host a nadir-pointing high-frame-rate video camera, relay synchronized position data and survey a region with sequential flights, each up to 20 min in duration. Videos frames were sorted into 120-frame bins and processed using the experimental fluid-lensing algorithm (Chirayath and Earle 2016) to remove refractive distortions caused by ambient surface waves. The corrected images and UAV position data were used as input frames for structure from motion to produce 2D, centimeter-scale orthophotos and a dense 3D bathymetry model. Calibration targets were distributed at varying water depths for georeferencing and bathymetry validation. Finally, terrestrial and millimeter-scale underwater gigapixel photogrammetry was performed to calibrate and verify 2D fluid-lensing reconstructions from airborne data, perform georectification, and validate derived 3D bathymetry. Where high-frequency Gaussian noise was present in the raw bathymetry as a result of resolution limitations, depth grids were low-pass filtered to 10- to 30-cm grid scale.

TABLE 1. Notation.

Symbol	Description	Unit
$\langle\cdot\rangle$	Spatial average	—
$\overline{(\cdot)}$	Time average	—
a_1	Linear roughness coefficient	—
A	Projected frontal area of object	m^2
A_b	Wave excursion distance	m
C_D	Bottom drag coefficient	—
$C_{D,B}$	Bulk (total) bottom drag coefficient	—
$C_{D,p}$	Pressure (form) drag coefficient	—
$C_{D,\tau}$	Skin friction drag coefficient	—
$D(x, t)$	Water depth	m
f_D	Total drag stress	Pa
$f_{\tau,b}$	Time-averaged bottom shear stress	Pa
$f_{p,b}$	Time-averaged stress from bottom pressure	Pa
$f_x(x, b)$	Smoothing function with tapering scale b	—
$\mathcal{F}_D$	Total drag force	N
$F_{\tau,b}$	Acceleration from near-bed shear stress	$m\,s^{-2}$
$F_{p,b}$	Acceleration from near-bed normal pressure	$m\,s^{-2}$
F_{PG}	Uniform pressure gradient acceleration	$m\,s^{-2}$
g	Gravitational acceleration	$m\,s^{-2}$
$h(x)$	Mean water depth	m
h_b	Physical scale of roughness elements	m
H_{rms}	Average rms wave height	m
L, W	Domain length (x) and width (y)	m
N_x, N_y, N_z	Number of model cells in x, y, z	—
$(\mathbf{n}, \mathbf{s})$	Unit normal and parallel vectors to bottom	—
p	Dynamic pressure	Pa
p_{nh}	Nonhydrostatic pressure	Pa
$\mathbf{q}(q_x, q_y)$	Flow	$m^2\,s^{-1}$
Re_D	Reynolds number relative to D	—
Re_h	Reynolds number relative to h_b	—
Re_w	Reynolds number relative to w	—
S	Radiation stress tensor	$kg\,s^{-2}$
$S_{dz'/dx}$	Spectral energy density of bottom slope	—
$S_{z'}$	Spectral energy density of bottom surface	m^2
$S_{\eta\eta}$	Power spectral density of free surface	$m^2\,Hz^{-1}$
T	Mean wave period	s
$\mathbf{u}(u, v, w)$	Mean Lagrangian velocity	$m\,s^{-1}$
$\mathbf{u}_E$	Eulerian velocity	$m\,s^{-1}$
$\langle u\rangle_H$	Spatially averaged u in horizontal (x, y) plane	$m\,s^{-1}$
u_*	Shear velocity	$m\,s^{-1}$
$\mathbf{U}(U, V, W)$	Depth-averaged Lagrangian velocity	$m\,s^{-1}$
$\mathbf{U}_{10}$	Wind speed at 10-m height	$m\,s^{-1}$
U_B	Spatially averaged velocity over domain	$m\,s^{-1}$
$\forall$	Model domain volume	m^3
$\mathbf{x}(x, y, z)$	Streamwise, spanwise, vertical coordinates	m
$\Delta x_G, \Delta y_G, \Delta z_G$	Model grid resolution in x, y, z	m
$\Delta x_B, \Delta y_B, \Delta z_B$	Bathymetric grid resolution in x, y, z	m
z'	Deviation of bottom surface	m
$z_{0,ur}$	Unresolved hydrodynamic roughness scale	m
z_0	Hydrodynamic roughness scale	m
$\tilde{z}$	Height above bottom or average depth	m
η	Free surface deviation	m
η_0	Mean water surface offset relative to datum	m
κ	Von Kármán's constant	—
$\boldsymbol{\lambda}(\lambda_x, \lambda_y)$	Characteristic bedform wavelength in x, y	m
ν	Molecular viscosity	$m^2\,s^{-1}$
ν_T	Turbulent eddy viscosity	$m^2\,s^{-1}$
Π	Cole's wake strength	—
ρ_0	Background density	$kg\,m^{-3}$
ρ	Water density	$kg\,m^{-3}$
τ_b	Bottom stress	Pa
τ_s	Surface stress	Pa

c. 3D nonhydrostatic model

The Stanford Unstructured Nonhydrostatic Terrain-following Adaptive Navier–Stokes Simulator (SUNTANS) modeling framework is a three-dimensional nonhydrostatic RANS model under the Boussinesq approximation (Fringer et al. 2006). The model grid is implemented in a rectangular horizontal grid with z-level vertical coordinate with domain length L, width W, average depth $\langle D\rangle$, and model grid spacing Δx_G, Δy_G, Δz_G. To compute the turbulent viscosity ν_T, a 3D k–ϵ turbulence model is employed within the generic length scale framework (Warner et al. 2005) with molecular viscosity $\nu = 1 \times 10^{-6}\,\mathrm{m^2\,s^{-1}}$. Time stepping is third-order Adams–Bashforth, and nonlinear momentum advection is central differencing. Initial conditions are zero velocity with uniform density. To achieve an equilibrium boundary layer, boundary conditions are periodic in the streamwise (x) direction and free slip on the lateral boundaries and free surface. The bottom boundary condition is a quadratic drag law with roughness height $z_{0,ur}$, imposed on the bottom grid cell (Fringer et al. 2006). For reef simulations, we assume $z_{0,ur} = 0.033$ cm, a value typically used for sand. The model is forced with a uniform pressure gradient, which is adjusted in time to achieve a desired domain-averaged velocity U_B (Nelson and Fringer 2017). Model simulations are run to steady state, typically at least five flow-through periods. The bathymetry for the reef simulations is linearly detrended in x and y, to minimize edge effects, and is smoothed along the periodic edges using $f_x = 0.5\tanh[x - b - \min(x)] + 0.5\tanh[-x - b + \max(x)]$, where the tapering length scale $b = 2$ m. Simulations were conducted on a 64-core AMD workstation.

3. Field measurement results

a. Hydrodynamic conditions

During the observation period, tidal variation of the free surface η is ± 0.5 m, winds are light at less than $5\,\mathrm{m\,s^{-1}}$, and wave forcing on the forereef consists of several long-period swell events with H_{rms} exceeding 1 m that propagate toward the reef crest and break; and thus H_{rms} in the lagoon is quite small (Figs. 2a–d). The effect of tidally modulated wave forcing creates a pressure gradient that drives a tidally varying flow in the pool center (Fig. 2e). The drifter tracks show the large-scale flow field from the reef crest exits through low areas in the reef crest and channels (predominantly near H0), and the general flow patterns are consistent over tidal phase on multiple days (Fig. 1b).

b. Momentum balance

In shallow depths, the bottom stress is often approximated with (Grant and Madsen 1979; Feddersen et al. 2003; Lentz et al. 2017)

$$\boldsymbol{\tau}_b = \rho C_D \mathbf{U}_E |\mathbf{U}_E|, \tag{1}$$

where C_D is a local nondimensional drag coefficient that may depend on the flow environment and bottom roughness and ρ is the fluid density.

Flow on shallow reefs is governed by the depth-integrated momentum equations for $\mathbf{U}(U, V)$ given by (e.g., Mei et al. 2005)

$$\frac{\partial \mathbf{U}}{\partial t} + \mathbf{U}\cdot\nabla\mathbf{U} = -g\nabla\overline{\eta} - \frac{1}{\rho D}\left(\nabla\cdot\mathbf{S} + \overline{\boldsymbol{\tau}_b} - \overline{\boldsymbol{\tau}_s}\right), \tag{2}$$

where time-varying depth $D = \overline{\eta} + h$, h is mean depth, $\overline{\eta}$ is the mean free surface, $\mathbf{S}$ is the radiation stress tensor, g is gravitational acceleration, $\overline{\boldsymbol{\tau}_s}$ is the mean surface stress, and $\overline{f}$ is a time average of function f. In the alongshore (x) direction, neglecting $V\partial U/\partial y$, substituting (1), assuming the water surface slope is linear, flow $\mathbf{q} = \mathbf{U}D$, and by continuity the flow q_x does not change significantly along x_1 to x_2, and taking the spatial average of (2) from point x_1 to x_2, $\langle f\rangle = (1/L)\int_{x1}^{x2} f\,dx$,

$$\begin{aligned}\frac{\partial}{\partial t}\frac{q_x}{\langle D\rangle} + q_x^2\left\langle D^{-1}\frac{\partial}{\partial x}D^{-1}\right\rangle = &-\frac{g}{L}\left(\overline{\eta}_{x2} - \overline{\eta}_{x1}\right) - \frac{1}{\rho}\left\langle\left(\frac{\partial S_{xx}}{\partial x} + \frac{\partial S_{xy}}{\partial y}\right)D^{-1}\right\rangle \\ &- \frac{\langle C_D\rangle\overline{q_x|\boldsymbol{q}|}}{\langle D^3\rangle} + \frac{1}{\rho}\langle\overline{\tau_{sx}}D^{-1}\rangle.\end{aligned} \tag{3}$$

From left to right, the terms in (3) will be referred to as unsteady (US), nonlinear advection (NL), pressure gradient (PG), radiation stress gradient (RSG), bottom stress (BT), and surface stress (ST), where the local C_D given by (1) becomes the spatially averaged drag coefficient $\langle C_D\rangle = \langle C_D D^{-3}\rangle/\langle D^{-3}\rangle$. For field observations on shallow reefs, the momentum equation in integral form [(3)] is shown to have increased accuracy over the differential form [(2)] owing to its inclusion of the spatial depth variability between measurement points (Lentz et al. 2017).

In a turbulent channel flow where roughness elements are small compared to the depth, the velocity profile is well represented by the log-layer approximation:

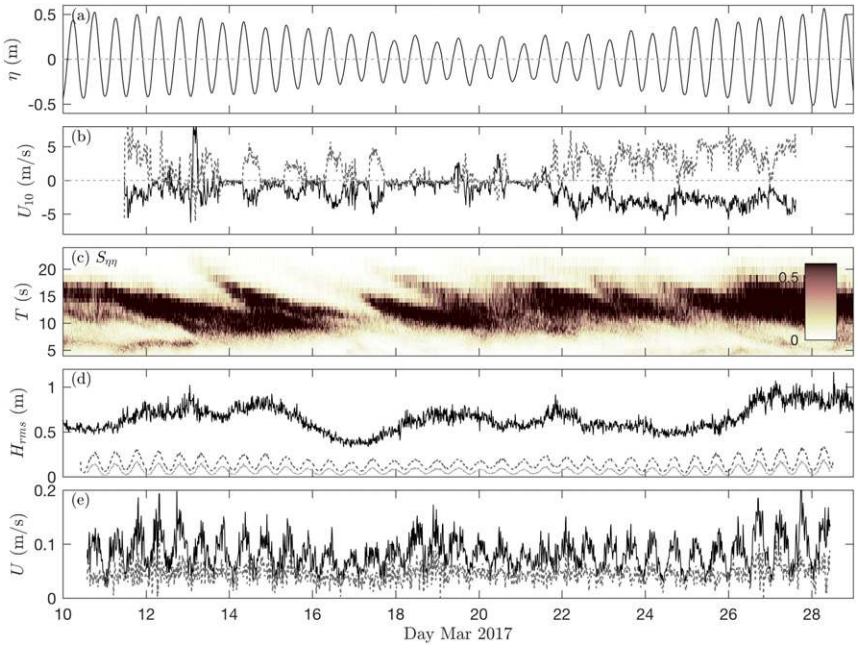

FIG. 2. Oceanic forcing conditions from March 2017 on Ofu Reef. (a) Tidal level η; (b) wind velocity $\mathbf{U}_{10}$ in AS (solid) and CS (dashed) directions; (c) wave power spectral density $S_{\eta\eta}$ ($m^2\,Hz^{-1}$) as a function of period T on forereef FR5; (d) rms wave height H_{rms} on forereef FR5 (solid), reef crest D-5 (dashed), and middle of pool 400 D0 (dotted–dashed); and (e) observed depth average velocities at site D0 in alongshore x (solid) and cross-shore y (dashed) directions.

$$u(\tilde{z}) = \frac{u_*}{\kappa}\left[\log\left(\frac{\tilde{z}}{z_0}\right) + 2\Pi\,\sin^2\left(\frac{\pi\tilde{z}}{2D}\right)\right], \qquad (4)$$

where the shear velocity $u_* = \sqrt{\tau_b/\rho}$, the height above the bottom $\tilde{z} = z + D$, z_0 is a hydrodynamic roughness scale, κ is von Kármán's constant (0.41), and Π is Cole's wake strength (~0.2 for high Reynolds number). Integrating (4) over the depth and substituting (1) (Lentz et al. 2017),

$$C_D = \kappa^2\left[\log\left(\frac{D}{z_0}\right) + (\Pi - 1)\right]^{-2}, \qquad (5)$$

which is valid for $D/z_0 > 10$. Given a velocity measurement bounded by two depth measurements and a horizontal profile of depth, (3) and (5) can be solved to determine an average z_0 for the profile (Lentz et al. 2017).

The mean water surface offset η_0 between the offshore and each site in the lagoon is based on solving (3) for low forcing conditions (see appendix) and shows a steep increase from the shallow outlet at K0 and a more gradual increase within the pool from site G0 to A0 (Fig. 3a). The time-averaged flow magnitude $|\mathbf{q}|$ generally increases along the pool to a maximum at H0 where much of the flow exits the pool (Figs. 1b and 3b).

The results for the spatially averaged $\langle C_D\rangle$ from the momentum balance vary along the transect between $O(0.01)$ and $O(0.1)$ (Fig. 3c). Comparing to the results using a logarithmic fit to the velocity profile in (4) and the Reynold's stress method (appendix, Eq. A2), $\langle C_D\rangle$ are similar magnitude but fall outside the 95% confidence limits (Fig. 3c). The likely explanation for this is that $\langle C_D\rangle$ is averaged over $O(100)$ m, while the log fit and Reynold's stress methods are local measurements. The spatially averaged roughness scale z_0 from the momentum balance varies from $O(1)$ to $O(10)$ cm along the transect, and results from the local log fit are similar (Fig. 3d). Time-average velocity profiles normalized by the depth-averaged velocity show a logarithmic profile within the midwater column (Fig. S2). This confirms the applicability of (4) for determining a local roughness value. At the two deeper sites (B0, D0) the profile is logarithmic over the measured depth, but at the two shallower sites (F0,H0) the profile deviates from a logarithmic profile below 0.3 and above 0.6 $\tilde{z}/D$, likely caused by the large roughness elements relative to depth. It is possible that some of the deviations are due to inaccurate reference height $\tilde{z}$, which on reefs is sometimes accounted for with an additional offset variable in (4) (Rosman and Hench 2011).

The magnitude of the terms in (3) shows the leading terms are between pressure gradient (PG) and bottom stress (BT), while the NL and RSG terms may become

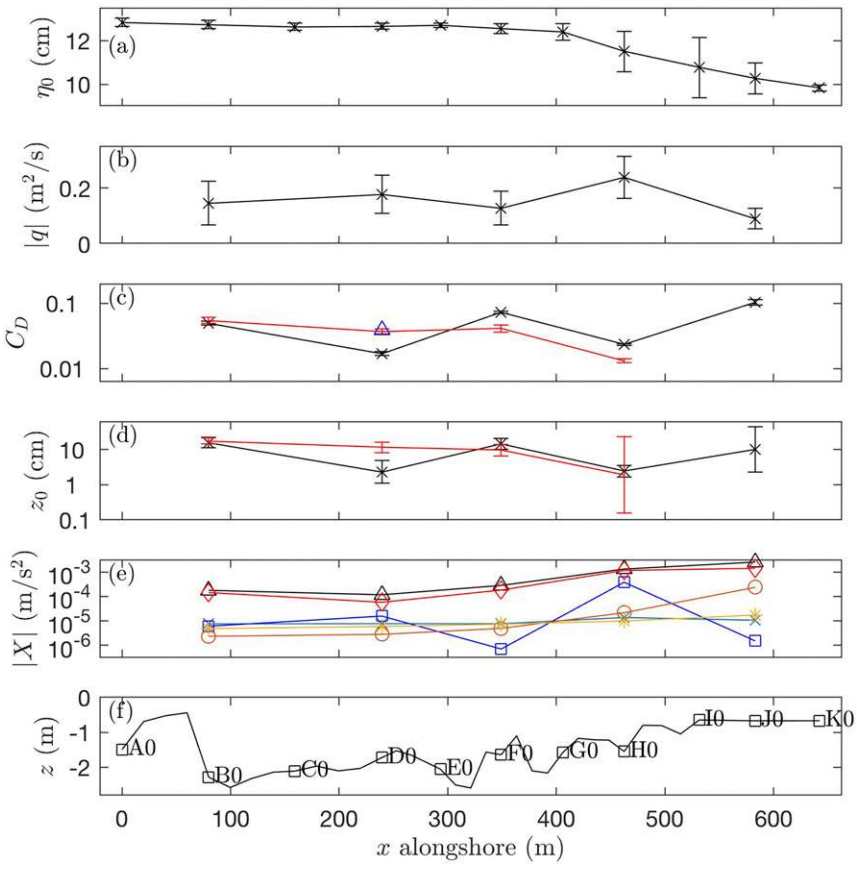

FIG. 3. Mean water level setup and drag results along centerline of pool 400. (a) Mean water level setup η_0 relative to offshore; (b) mean flow |q|; (c) drag coefficient C_D from spatially averaged C_D from momentum balance in (3) (black x), local C_D from least squares fit of (4) (red dash), and local C_D from Reynolds stress in (A2) (blue triangle); (d) hydrodynamic roughness z_0, with colors as in (c); (e) magnitude of terms in momentum balance in (3), US (cyan x), NL (blue square), PG (black triangle), RSG (orange circle), BT (red diamond), and ST (yellow asterisk); and (f) depth below mean surface z showing measurement stations A0–K0. Error bars are 90% confidence intervals of the mean.

of secondary importance in some locations. (Fig. 3e). Thus, in this study site, (3) can be simplified to

$$0 = -\frac{g}{L}\left(\overline{\eta}_{x2} - \overline{\eta}_{x1}\right) - \frac{\langle C_D\rangle\overline{q_x|\boldsymbol{q}|}}{\langle D^3\rangle}. \tag{6}$$

For this work, we ignore the effects of waves on creating a rougher boundary layer and influencing C_D. For this site, with mean flows U of $O(0.1)\,\mathrm{m\,s^{-1}}$, the relatively small wave heights in the pool (Fig. 2) create wave excursion distances A_b of $O(0.2)$ m, and wave velocities of $O(0.1)\,\mathrm{m\,s^{-1}}$. Considering the physical scale of roughness elements h_b is typically 1 m, the relative excursion $A_b/h_b < 1$, and ratio of wave velocities to mean currents is $O(1)$ or less. For flows in this regime, the effect of waves may create a rougher boundary layer height (Lentz et al. 2017). However, considering the high uncertainty for some of the field sites in the results for z_0 (Fig. 3d), we consider this a second-order effect.

4. Theory and model results

a. Theoretical approach

To better understand the detailed flows in this environment and extend beyond the limited field observation sites, we model the complex flows on the reef using the detailed bathymetric measurements. We apply the SUNTANS modeling framework in periodic boundary conditions forced by a uniform pressure gradient acceleration F_{PG} in an unstratified fluid in a nonrotating frame. The momentum and continuity model equations are

$$\frac{\partial \mathbf{u}}{\partial t} + \mathbf{u}\cdot\nabla\mathbf{u} = -\frac{1}{\rho_0}\nabla p - \frac{g}{\rho_0}\rho\mathbf{k} + \nabla\cdot(\nu_T\nabla\mathbf{u}) + F_{\mathrm{PG}}\,, \quad (7)$$

and

$$\nabla\cdot\mathbf{u} = 0, \quad (8)$$

where $\mathbf{u} = (u, v, w)$ is the velocity vector, p is the dynamic pressure composed of a nonhydrostatic and hydrostatic component ($p = p_{\mathrm{nh}} + \rho_0 g\eta$), and background density $\rho_0 = 1000\,\mathrm{kg\,m^{-3}}$.

Upon time (t) averaging, domain volume ($\forall$) averaging, invoking Gauss's theorem, and assuming steady state, the x component of (7) becomes the following:

$$F_{\mathrm{PG}} = \frac{1}{\rho_0}\left\langle\frac{f_{\tau,b}}{D}\right\rangle + \frac{1}{\rho_0}\left\langle\frac{f_{p,b}}{D}\right\rangle = F_{\tau,b} + F_{p,b}, \quad (9)$$

where $f_{\tau,b}$ is the time-average bottom shear stress and $f_{p,b}$ is the stress from mean pressure acting on the bottom (indicated by the subscript b). Note this is an analogous statement to (6), that is, that a mean pressure forcing balances stresses on the bottom. However, (9) separates the stresses on the bottom into shear stress and pressure stress, which creates form drag. The $F_{\tau,b}$ is the acceleration due to the mean velocity parallel to the bottom:

$$F_{\tau,b} = \frac{1}{D}\left(\nu_T\nabla\overline{\mathbf{u}}_b\cdot\mathbf{n}\right), \quad (10)$$

where the bottom following coordinate system ($\mathbf{n}$, $\mathbf{s}$) are the unit normal and unit parallel bottom surface vectors, respectively. The $F_{p,b}$ is due to the bottom pressures acting normal to the bottom and computed from (9). Normalizing (9) by density times the mean depth over twice the kinetic energy ($\rho_0\langle D\rangle/\rho_0 U_B^2$) gives drag coefficients due to the total (bulk) flow, shear stress, and form drag in the streamwise direction:

$$F_{\mathrm{PG}}\frac{\langle D\rangle}{U_B^2} \equiv \left\langle C_{D,B}\right\rangle = \left\langle C_{D,\tau}\right\rangle + \left\langle C_{D,p}\right\rangle. \quad (11)$$

b. Model validation and results

While RANS models have shown effectiveness in computing hydrodynamic flows and drag coefficients at a range of scales, previous studies note some limitations in computing the details of turbulence and eddy formation especially for bluff bodies where the details of flow separation are important (Rodi 1997; Lübcke et al. 2001). To validate the hydrodynamic model, a series of three idealized simulations on a cylinder, cube, and sinusoidal bottom are conducted with known experimental results (Table 2) in addition to validation on the Ofu reef presented next (Table 3).

The simulations are conducted at Re similar to those expected on the field site, where mean velocities are on average $O(0.1)\,\mathrm{m\,s^{-1}}$ (Fig. 2). The horizontal width w of the dominant bottom features are $O(1)$ m (Figs. 4 and 5). Thus, at the site, the average $\mathrm{Re}_w = (U_B w)/\nu = 1\times10^5$ but can vary from 6×10^4 to 1×10^6.

To compare to results from the literature, $C_{D,B}$ for the cylinder and cube simulations are computed by $C_{D,B} = 2\mathcal{F}_D/\rho U_B^2 A$, with total drag force $\mathcal{F}_D = \rho\forall F_{\mathrm{PG}}$ and projected frontal area A. For the cylinder simulation $\mathrm{Re}_w = 1\times10^5$, and $C_{D,B}$ is within 5% of the published value (Kundu and Cohen 2008) (Table 2). For higher $\mathrm{Re}_w = 5\times10^6$, where we expect transition to a turbulent boundary layer and decrease in the net drag, the model result overpredicts $C_{D,B}$ by 42% (Roshko 1961) (Table 2). For the cube simulation, the model result for $C_{D,B}$ is within 5% of the published value and not a function of Re_w (Bearman 1971) (Table 2). For the sinusoidal bathymetry $\mathrm{Re}_D = (U_B D)/\nu = 4.2\times10^5$ and using (11) to compute $\langle C_{D,B}\rangle$, which is within 18% of the experimental result (Gong et al. 1996) and within 36% of the LES simulation result (Salvetti et al. 2001) (Table 2).

Thus, the model accurately computes the drag coefficients for a range of rounded and sharp surfaces at Re typical of the study site. For forms with rounded features such as a cylinder at $\mathrm{Re_w}$ greater than 5×10^5, the model may overpredict the drag coefficient. However, the typical $\mathrm{Re_w}$ on this reef is 1×10^5, below this threshold. In addition, many of the forms on the reef have sharp edges and the drag coefficient is not expected to vary with Re.

The reef surface is modeled using a similar approach as the idealized domains (Table 3). Model results at site D0 with rounded isolated roughness elements show strong horizontal variability in the flow field near the bottom with separated wakes in both the horizontal and vertical (Figs. 4a,d). The aerial image shows the roughness elements at this site are Porites corals surrounded by sand (Fig. 4b). The pressure field shows corresponding high pressures in the front of the roughness elements (some from the free surface $\overline{\eta}$ and the remainder from nonhydrostatic pressure), with negative pressures in the lee-separated wake regions, leading to a net form drag (Figs. 4c,f). Eddy diffusivity is highest in the interior and is highly turbulent $O(10)\,\mathrm{cm^2\,s^{-1}}$ (Fig. 4e), similar to field measurements on other reefs (Reidenbach et al. 2006). The separated wakes are qualitatively similar in flow direction and extent of separation to detailed field observations on other reefs (Hench and Rosman 2013).

Model results at site F0, which has more irregular bathymetry, are similar, but the wakes behind the roughness elements and resulting pressure field are

TABLE 2. Idealized hydrodynamic model simulations. Note that for all simulations $\nu = 1 \times 10^{-6}\,\mathrm{m^2\,s^{-1}}$ and $z_{0,ur} = 0.0001$ cm.

	L, W, D (m)	N_x, N_y, N_z	U_B (cm s^{-1})	Re[a]	Model $C_{D,B}$[b]	Expt $C_{D,B}$[b]
Cylinder (diameter = 5 m; height = 3.75 m)	30, 15, 7.5	120, 60, 80	2.0	1×10^5	1.15	1.2[c]
			100	5×10^6	1.07	0.75[c]
Cube (width = 5 m; height = 3.75 m)	30, 15, 7.5	120, 60, 80	2.0	1×10^5	1.15	1.2[d]
Sinusoidal (amplitude = 1.19 m; wavelength = 15 m)	30, 30, 15	60, 60, 80	2.78	4.2×10^5	0.015	0.011[e], 0.013[f]

[a] For cylinder and cube $\mathrm{Re}_w = U_B w/\nu$, for sinusoidal $\mathrm{Re}_D = U_B D/\nu$.
[b] For cylinder and cube $C_{D,B}$ is the local drag coefficient, and for sinusoidal $C_{D,B}$ is the volume-averaged drag coefficient $\langle C_{D,B}\rangle$.
[c] Kundu and Cohen (2008).
[d] Roshko (1961).
[e] Gong et al. (1996).
[f] Salvetti et al. (2001).

larger and dominated by the large-scale features (Figs. 5a,c,d,e,f). The aerial image shows this site has smaller irregular coral shapes with some sand patches (Fig. 5b).

The model results for $\langle C_{D,B}\rangle$ generally show good agreement with the field observations, although with a high degree of scatter (Fig. 6). The high degree of scatter is likely due primarily to the spatial scales of the different results. The model simulations are conducted at 20–32-m spatial scale owing to model time and bathymetric limitations. The field results are averaged over $O(100)$ m for the results from the momentum equation, but are local measurements for the logarithmic fit and Reynolds stress methods. Thus, while there is scatter in these results, the validation confirms that this model reasonably computes $\langle C_{D,B}\rangle$ on these reef surfaces and can be applied to additional model scenarios and reef locations.

c. Drag

Given shallow steady unidirectional flow over a periodic wavy bathymetric surface, the relevant variables are a resisting drag force over area (stress) f_D, depth-averaged flow U_B, average depth D, characteristic bottom height h_b, characteristic bedform wavelength in the direction parallel and normal to flow (λ_x, λ_y), fluid density ρ, and fluid viscosity ν. Per Buckingham pi theorem a common way to nondimensionalize this problem is the following (Grant and Madsen 1982; Wooding et al. 1973):

$$C_{D,B} = \frac{f_D}{\rho U_B^2} = f\left(\mathrm{Re}_h, \frac{D}{h_b}, \frac{h_b}{\lambda_x}, \frac{h_b}{\lambda_y}\right). \tag{12}$$

At high Reynolds numbers ($\mathrm{Re}_h = h_b U_B/\nu > 10^6$), the flow is in the rough turbulent regime and the $C_{D,B}$ should be independent of Re_h, while in the turbulent transition regime, $C_{D,B}$ should vary like $C_{D,B} \propto \mathrm{Re}_h^{-1/7}$ (Schlichting 1979). For high relative depth (D/h_b) the flow profile is a well-developed log layer and (4) applies, while at low relative depth the roughness elements take up a significant part of the water column and the flow approaches a porous media flow (Rosman and Hench 2011; Lentz et al. 2017). At small bedform steepness in the direction of flow ($h_b/\lambda_x < 0.1$) there is no wake separation behind the bedforms and the drag is primarily due to skin friction, while at high bedform steepness wake separation is pronounced and the drag is primarily due to pressure form drag (Grant and Madsen 1982; Schlichting 1979). The last parameter h_b/λ_y is a spanwise steepness factor and governs how much of the flow is blocked; $C_{D,B}$ is at a maximum for high steepness factors (2D bedforms normal to flow) as a result of high pressure form drag, and $C_{D,B}$ decreases to skin friction for low steepness factors approaching 0 (2D bedforms aligned with flow).

TABLE 3. Reef hydrodynamic model simulations' base condition. Note that Var = varies, $\mathrm{Re}_h = \langle h_b\rangle U_B/\nu$, and for all simulations $\nu = 1 \times 10^{-6}\,\mathrm{m^2\,s^{-1}}$, $z_{0,ur} = 0.033$ cm, and $\Delta x_G = \Delta x_B$.

Site location	$L, W, \langle D\rangle$ (m)	$\Delta x_G, \Delta y_G, \Delta z_G$ (cm)	U_B (cm s^{-1})	Re_h	$\langle D\rangle/\langle h_b\rangle$	$\langle h_b\rangle/\langle \lambda_x\rangle$	$\langle h_b\rangle/\langle \lambda_y\rangle$
B0	18, 24, 1.81	30, 30, 3.5	4.9	7.0×10^4	1.27	0.24	0.23
D0	32, 16, 1.60	10, 10, 2.7	8.8	4.6×10^4	3.03	0.16	0.15
D-2	32, 16, 1.30	10, 10, 2.7	4.0	2.4×10^4	2.15	0.20	0.19
F0	20, 20, 1.20	10, 10, 3.1	5.5	4.1×10^4	1.61	0.29	0.22
H0	16, 12, 1.30	10, 10, 2.3	10.5	4.5×10^4	3.03	0.15	0.19
M1–M15	32, 16, Var	30, 30, Var	Var	4.6×10^4	3.03	Var	Var

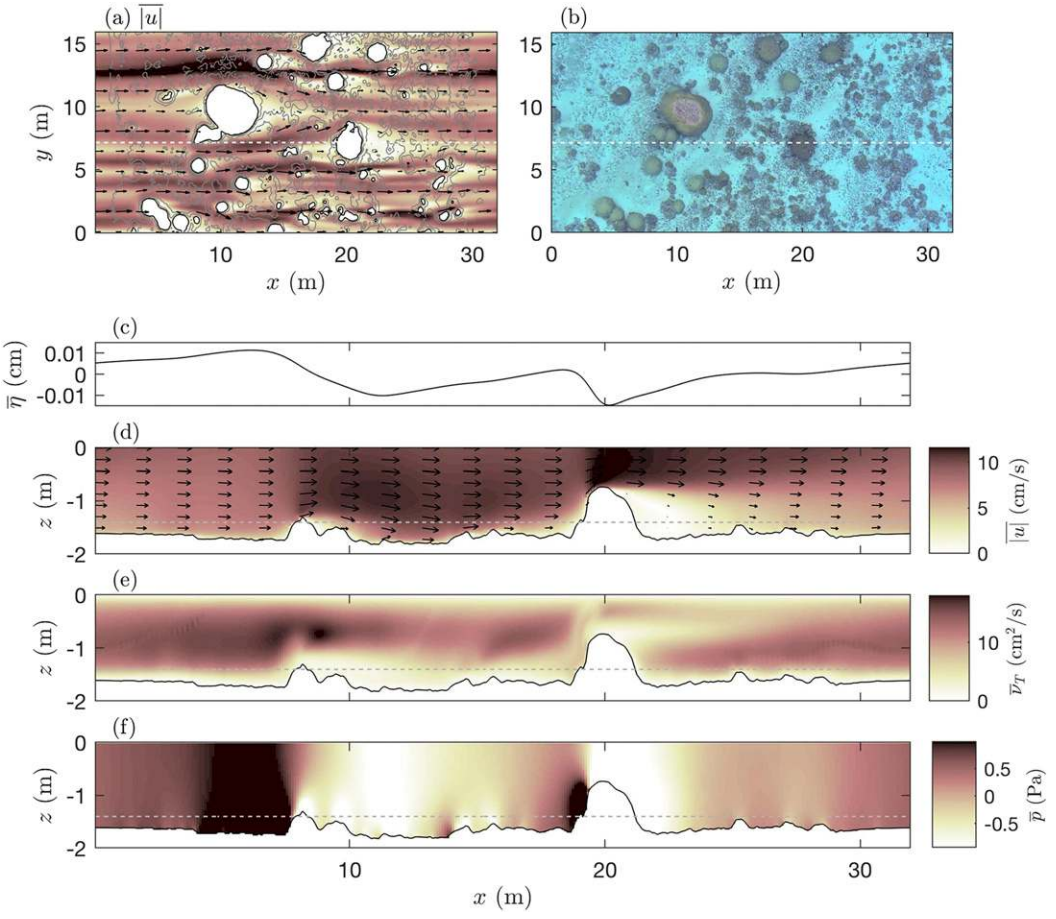

FIG. 4. Hydrodynamic model results at site D0 with large isolated coral heads showing wake separation and pressure distribution. (a) Top-down view showing mean velocity ($\overline{u}$, $\overline{v}$) around coral heads, (b) aerial image showing coral heads and sand, (c) profile of mean water surface $\overline{\eta}$, (d) side view of mean velocity ($\overline{u}$, $\overline{w}$) showing separated boundary layer and wake, (e) mean eddy diffusivity $\overline{\nu}_T$, and (f) side view of mean pressure $\overline{p}$. Contours in (a) only shown for reef surface below plane. Dashed lines in (a) and (b) represent (y = 7.15 m) location of (c)–(f), and dashed lines in (c)–(f) represent (z = −1.40 m) location of (a). Color scale for (a) is as in (c), and velocity vector scale in (a) and (d) is 15 cm s^{-1}.

We approximate the complex reef surface as multiple wavy bedforms superimposed together. The spatially averaged drag is then given by the spatial average of (12):

$$\left\langle C_{D,B} \right\rangle = f\left(\mathrm{Re}_h, \frac{\langle D \rangle}{\langle h_b \rangle}, \left\langle \frac{h_b}{\lambda_x} \right\rangle, \left\langle \frac{h_b}{\lambda_y} \right\rangle \right), \tag{13}$$

where $\langle D \rangle$ is the volume-averaged depth and $\mathrm{Re}_h = \langle h_b \rangle U_B / \nu$, and we have assumed $z'/\langle D \rangle \ll 1$ for the second term to be uncorrelated. The terms in (13) can be approximated assuming equivalent parameters to a wavy sinusoidal surface using the root-mean-square of the surface and the bottom slope:

$$\langle h_b \rangle = 2\sqrt{2}(z')_{\mathrm{rms}}, \quad \text{and} \tag{14}$$

$$\left\langle \frac{h_b}{\lambda} \right\rangle = \frac{\sqrt{2}}{\pi} \left(\frac{dz'}{d\mathbf{x}} \right)_{\mathrm{rms}}, \tag{15}$$

where $z'(x, y) = -[D(x, y) - \langle D \rangle]$ is the deviation of the bottom surface, D is detrended (no mean or mean slope), and the spatial root-mean-square operator $(f)_{\mathrm{rms}} = \langle f^2 \rangle^{1/2}$ is applied over the model domain. For this study, (14) and (15) are applied to the bathymetry at the same grid resolution as the model (Δx_G). The model grid depths are taken as the average of all subgrid-scale points from the high-resolution bathymetry (Δx_B).

The model is used to explore the variability of the terms in (13). The Reynolds number Re_h is varied over the range of observed values from 10^4 to 10^5 by changing U_B and, as expected, has very little effect on $C_{D,B}$ (Fig. 7). Since the flow is in a turbulent regime, the

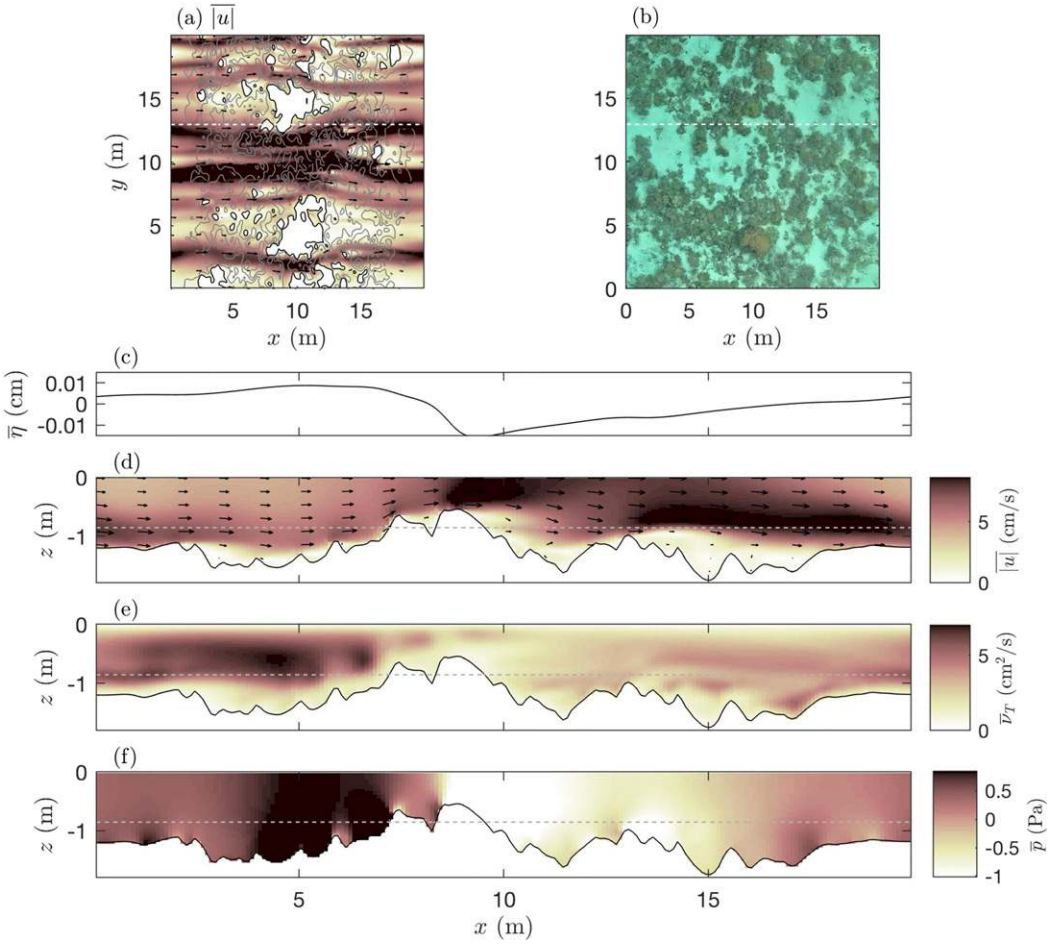

FIG. 5. Hydrodynamic model results at site F0 with small irregular corals showing wake separation and pressure distribution. Legend and notes are as in Fig. 4. Dashed lines in (a) and (b) represent ($y = 12.95$ m) location of (c)–(f), and dashed lines in (c)–(f) represent ($z = -0.83$ m) location of (a). Velocity vector scale in (a), (c), and (d) is 10 cm s^{-1}.

irregular forms of the reef create separated boundary layers (Figs. 4 and 5), which are not dependent on Re_h.

The relative depth $\langle D\rangle/\langle h_b\rangle$ is varied by changing $\langle D\rangle$ at sites D0 and F0 over the range of observed values. Both sites show decreasing $\langle C_{D,B}\rangle$ with increasing $\langle D\rangle/\langle h_b\rangle$, consistent with the theory in (5) (Fig. 8). This trend is primarily a result of $\langle C_{D,p}\rangle$ changing, while $\langle C_{D,\tau}\rangle$ remains very small over these simulations. Equation (5) matches the model results well for high relative depth (site D0) while somewhat underpredicting the drag at smaller relative depth (site F0).

The variation in relative slope $\langle h_b/\lambda_x\rangle$ is achieved by simulating many different model sites, while holding $\mathrm{Re_h}$ and $\langle D\rangle/\langle h_b\rangle$ constant (the same as site D0 base case) (Fig. 9). The $\langle C_{D,B}\rangle$ increases linearly for $\langle h_b/\lambda_x\rangle > 0.05$ because of an increase in $C_{D,p}$. For idealized sinusoidal forms, flow separation and high form drag occur at $h_b/\lambda_x > 0.1$ (Salvetti et al. 2001), but the reef model results show a dominance in form drag for $\langle h_b/\lambda_x\rangle > 0.05$, likely since the irregular reef bedforms create more flow separation at a lower average slope. At very low slopes, $\langle C_{D,p}\rangle$ trends toward zero and $\langle C_{D,\tau}\rangle$ becomes the dominant term in (13). These simulations are of a highly smoothed spatially downsampled reef ($\Delta x_G > 3$ m) with the model grid resolution the same as the bathymetry. Thus for this reef, form drag due to pressure $\langle C_{D,p}\rangle$ is the dominant term at all sites.

In Fig. 9, there is some variability in $\langle h_b/\lambda_y\rangle$ that cannot be independently varied. But, because most reef surfaces at this scale are symmetric, $\langle h_b/\lambda_x\rangle$ and $\langle h_b/\lambda_y\rangle$ are typically of similar order (Fig. 10a). Thus, $\langle h_b/\lambda_y\rangle$ is not expected to be a significant parameter in predicting $\langle C_{D,B}\rangle$, a simplification also used in studies on sediment bedforms (Wooding et al. 1973; Grant and Madsen 1982). However, for forms that are not symmetric it could become an important factor.

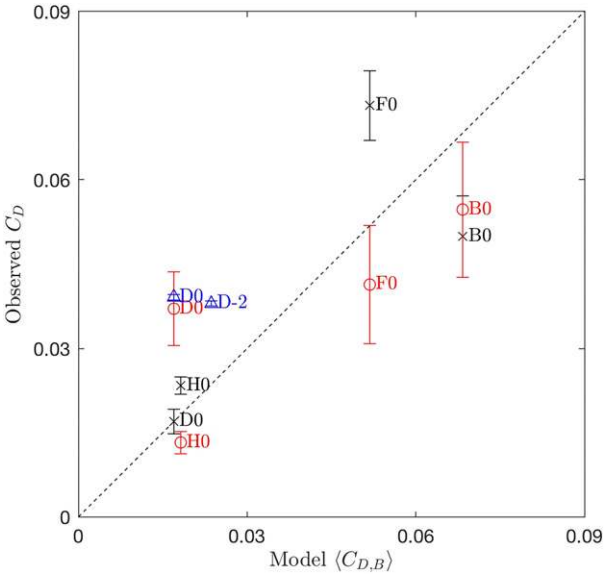

FIG. 6. Comparison of model computed total drag coefficient $\langle C_{D,B}\rangle$ and field observations for field sites on shallow reef. Black x is $\langle C_{D,B}\rangle$ from bulk pressure gradient from (3), red circle is C_D from log fit to local velocity profile from (4), and blue triangle is C_D from near-bed Reynold's stress from (A2). Model simulations are run at average depth and flow velocities at each site (Table 3).

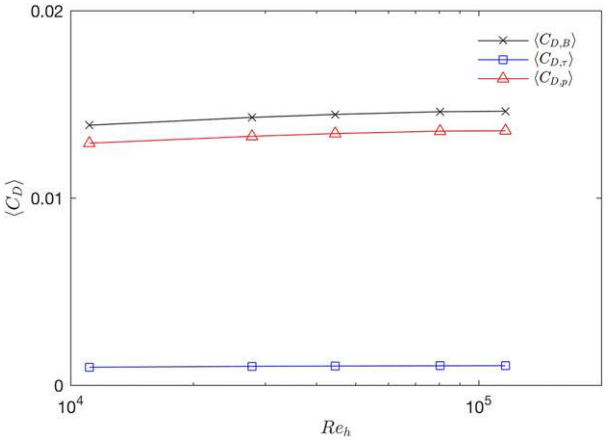

FIG. 7. Dependence of total $\langle C_{D,B}\rangle$, shear $\langle C_{D,\tau}\rangle$, and form $\langle C_{D,p}\rangle$ drag coefficients on Reynolds number $\mathrm{Re}_h = U_B\langle h_b\rangle/\nu$ for range of observed flows at site D0. Note relative depth $\langle D\rangle/\langle h_b\rangle$ and average steepness $\langle h_b/\lambda_x\rangle$ are held constant for these simulations.

Finally, in all the simulations we have assumed unidirectional flow, and the factor $\langle h_b/\lambda_x\rangle$ is not dependent on the sign of the flow. However, it is well known that, because of flow separation, a bluff body will have less form drag if it has an abrupt front and gently sloping lee rather than a gentle front and abrupt lee (Kundu and Cohen 2008). We vary the flow direction on a square domain (32 m × 32 m) at site D0. The $\langle C_{D,B}\rangle$ varies slightly with flow direction by up to 7% (Fig. 10b). As a result, we consider flow sign a minor effect for these reef surfaces, which are primarily symmetric.

Thus, the important terms in (13) are the relative depth and slope in the streamwise direction, and (13) simplifies to

$$\left\langle C_{D,B}\right\rangle = f\left(\frac{\langle D\rangle}{\langle h_b\rangle}, \left\langle\frac{h_b}{\lambda_x}\right\rangle\right). \tag{16}$$

d. Hydrodynamic length scales

For a well-developed turbulent flow, the characteristic hydrodynamic length scale for k–δ-type roughness (Wooding et al. 1973) should be proportional to the following (Grant and Madsen 1982; Nielsen 1992):

$$z_0 = f\left(h_b\frac{h_b}{\lambda_x}\right), \tag{17}$$

where h_b is the roughness height and h_b/λ_x is the roughness spacing or the roughness slope. A reasonable parameterization for (17) for periodic bedforms is given by $z_0 = a_1 h_b(h_b/\lambda_x)$, and previous experimental results found a_1 equal to 0.27 for sand ripples (Nielsen 1992), 0.36 for triangular ripples (Jonsson and Carlsen 1976), 0.50 for the atmospheric boundary layer (Lettau 1969), and 0.83 (Swart 1977) and 0.92 (Grant and Madsen 1982) for oscillatory flow over ripples. For complex terrain, we propose to approximate the roughness height by $\langle h_b\rangle$ and the roughness concentration by $\langle h_b/\lambda_x\rangle$, and (17) becomes

$$\langle z_0\rangle = a_1\langle h_b\rangle\langle h_b/\lambda_x\rangle + \langle z_{0,ur}\rangle, \tag{18}$$

where $\langle z_{0,ur}\rangle$ is the contribution from the unresolved hydrodynamic roughness, at scales smaller than the measurement resolution. Substituting spatial averages into (5),

$$\langle C_{D,B}\rangle = \kappa^2\left[\log\left(\frac{\langle D\rangle}{\langle z_0\rangle}\right) + (\Pi - 1)\right]^{-2}. \tag{19}$$

Substituting (18) into (19), the term $\langle D\rangle/\langle z_0\rangle$ becomes

$$\frac{1}{a_1}\frac{\langle D\rangle}{\langle h_b\rangle}\left\langle\frac{h_b}{\lambda_x}\right\rangle^{-1}.$$

Thus, (18) and (19) contain the important nondimensional parameters in (16) concluded from the model results. While the current study uses downsampled bathymetry with a grid spacing equal to the model grid ($\Delta x_G = \Delta x_B$) to estimate a_1, in practice, for estimating hydrodynamic roughness this method should apply (18) to bathymetric data at the highest available resolution, which should be higher than the model resolution. For

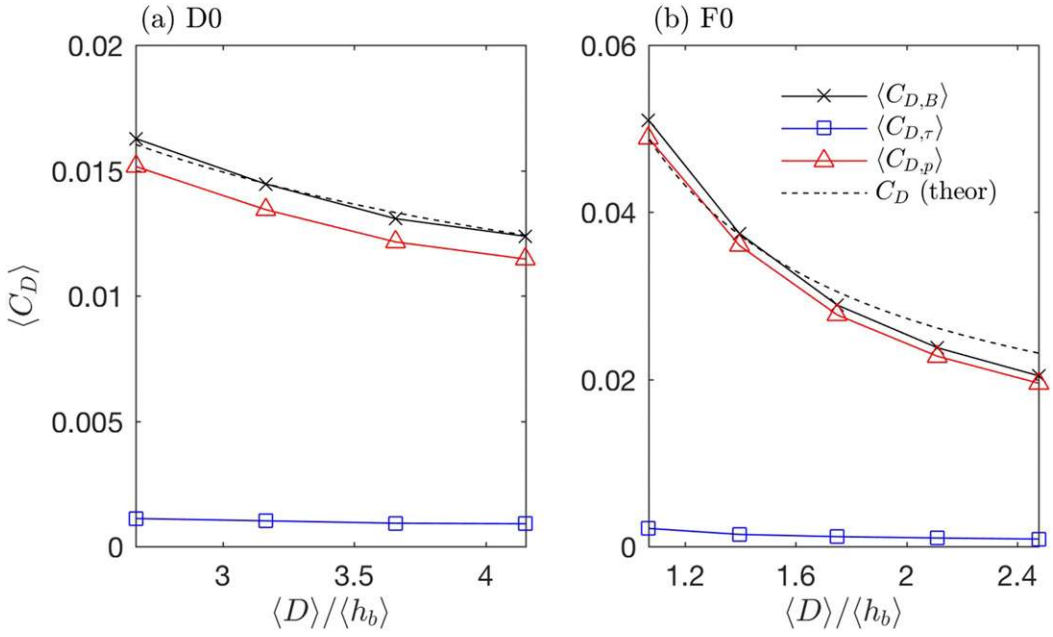

FIG. 8. Dependence of drag coefficients on relative depth $\langle D \rangle / \langle h_b \rangle$ at sites D0 and F0, comparing model results for total $\langle C_{D,B} \rangle$, shear $\langle C_{D,\tau} \rangle$, and form $\langle C_{D,p} \rangle$ drag, compared to least squares fit of (5) by changing z_0. Note for these simulations, steepness $\langle h_b/\lambda_x \rangle$ and Reynolds number $\mathrm{Re_h}$ are held constant.

irregular surfaces, a vertical step in the high-resolution bathymetry would give the singularity $\langle h_b/\lambda_x \rangle = \infty$ and the unphysical result $\langle z_0 \rangle = \infty$. In this case, the fundamental assumption of a wavy surface is violated, and some spatial smoothing may be required to apply (18).

An analysis of all model runs on the Ofu reef with a best fit of 41 model simulations to (18) and (19) gives $a_1 = 0.38$ with a coefficient of determination R^2 of 0.79 (Fig. 11). The results in Fig. 11 are based on results within $6 \times 10^3 < \mathrm{Re}_h < 7 \times 10^4$, $1.1 < \langle D \rangle / \langle h_b \rangle < 6.3$, and $0.7 < \langle h_b/\lambda_x \rangle < 0.29$. However, (18) is likely valid as long as the flow is turbulent; additionally the upper limit of $\langle D \rangle / \langle h_b \rangle$ approaching a pure boundary layer, and the lower limit of $\langle h_b/\lambda_x \rangle$ approaching a flat bottom are likely not limiting. The results for $\langle z_0 \rangle$ compare well to other studies on ideal sinusoidal forms (Salvetti et al. 2001; Zilker and Hanratty 1979; Buckles et al. 1984; Henn and Sykes 1999) and triangular ripples ($a_1 = 0.36$) (Jonsson and Carlsen 1976) but are somewhat higher than $\langle z_0 \rangle$ for sand ripples ($a_1 = 0.27$) (Nielsen 1992).

The vertical profiles of horizontal velocity at sites D0 and F0 show high horizontal variability in u but relatively similar profiles in horizontally averaged $\langle u \rangle_H$ when normalized by U_B above the mean depth ($\tilde{z}/\langle D \rangle) > 0$ (Fig. 12a), where $\tilde{z} = z + \langle D \rangle$ is upward from the mean depth. Values of $\langle u \rangle_H$ below the mean depth tend toward zero within the reef canopy and are highly variable depending on the reef bathymetry. Scaling all reef model simulations by $\tilde{z}/\langle D \rangle$ and scaling all horizontally averaged velocity $\langle u \rangle_H$ by U_B collapses the data into self-similar profiles (Fig. 12b). The profiles are logarithmic within the middle of the water column, as predicted by theory in (4). Thus, while the local velocity is highly variable, a spatial horizontal average $\langle u \rangle_H$ is well approximated by a log-layer parameterization above the mean depth.

A final question of interest is what horizontal spatial scales are most important on the reef for creating drag. A series of simulations at sites D0 and F0 are conducted by varying the bathymetry grid resolution Δx_B from 10 cm to 24 m, where the 24-m resolution is flat. Model grid resolution Δx_G is held constant at 10 cm, and a cubic spline method is used to interpolate from the coarser bathymetry grid to the finer model grid. The total drag $\langle C_{D,B} \rangle$ increases and then levels off with increasing grid resolution with $\langle C_{D,p} \rangle$ the primary component of this increase (Figs. 13a,b). At the highest modeled resolution, $\langle C_{D,B} \rangle$ approaches the field observed values, but as noted previously, there are inherent differences in the spatial averaging of these different methods. For the modeled bathymetry, the important result is that $\langle C_{D,B} \rangle$ is approaching an asymptotic value, where enhanced grid resolution is contributing little to the drag.

We use Fourier analysis of the bathymetry in the x direction with wavelength λ and the spectral energy density (SED) $S(\lambda)$averaged in the y direction applied

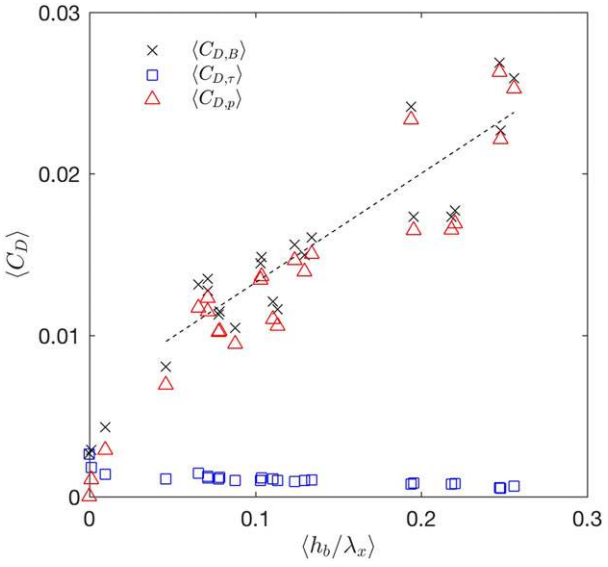

FIG. 9. Model results for results for total $\langle C_{D,B} \rangle$, shear $\langle C_{D,\tau} \rangle$, and form $\langle C_{D,p} \rangle$ drag as a function of spatially averaged slope $\langle h_b/\lambda_x \rangle$ at multiple sites. Note for these simulations, relative depth $\langle D \rangle/\langle h_b \rangle$ and Reynolds number $\mathrm{Re_h}$ are held constant. For very small $\langle h_b/\lambda_x \rangle < 0.05$, U_B and $\langle D \rangle$ are held constant with decreasing grid resolution; thus for these simulations $\langle D \rangle/\langle h_b \rangle$ and Re_h are not constant.

at different bathymetric grid resolutions Δx_B. SED of the depth $S_{z'}$ shows highest spectral density for the large-scale features and decreasing density for the small-scale features (Figs. 13c,d). SED of the streamwise bottom slope $S_{dz'/dx}$ shows increasing magnitude with smaller grid scales and a peak wavelength λ_x of approximately 4.5 and 1.1 m at sites D0 and F0, respectively (Figs. 13e,f), the same scale at which $\langle C_{D,p} \rangle$ begins to increase (Figs. 13a,b). Qualitative inspection of the coral forms in the plan view shows the spacing is of similar order (Figs. 4 and 5). Thus, $S_{dz'/dx}$ appears to be a good quantitative metric to identify the dominant horizontal length scales creating hydrodynamic drag. The grid spacing required to adequately resolve the wake effects and thus accurately model $\langle C_{D,p} \rangle$, appears to be approximately 11 (F0) to 45 (D0) times smaller than the spectral peak wavelength of $S_{dz'/dx}$ (Fig. 13).

The mean dynamic pressure field $\overline{p}$ at site D0 shows decreasing differences in $\overline{p}$ for larger grid scales (Fig. 14), which leads to the decrease in $\langle C_{D,p} \rangle$ (Fig. 13a). However, while there are some enhanced details in the near bed $\overline{p}$ at 10-cm resolution, the primary pressure features and magnitude remain similar between 10- and 30-cm resolution (Figs. 14a–c). The physical reason for this is that the large-scale features dominate the flow field, and smaller features are contained within the wakes and boundary layer created by the dominant scale features, a characteristic feature of k–δ-type roughness (Figs. 4 and 5). Thus, once the dominant hydrodynamic features are resolved with $O(10–50)$ grid cells, enhanced resolution has little effect on the drag.

5. Discussion

Based on field observations from a shallow reef in American Samoa, we compute spatially averaged drag coefficients at several sites, which are averaged over

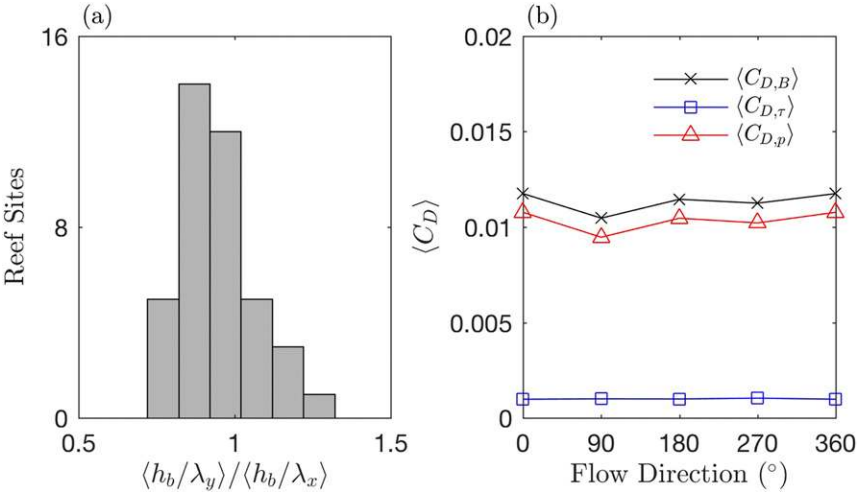

FIG. 10. Symmetry of reef bedforms and effect of flow direction reef sites. (a) PDF of ratio of spatially averaged slopes in the cross-flow (y) and streamwise (x) directions showing most reef forms are symmetric, and (b) variations in flow direction have little effect on total $\langle C_{D,B} \rangle$, shear $\langle C_{D,\tau} \rangle$, and form $\langle C_{D,p} \rangle$ drag at site D0.

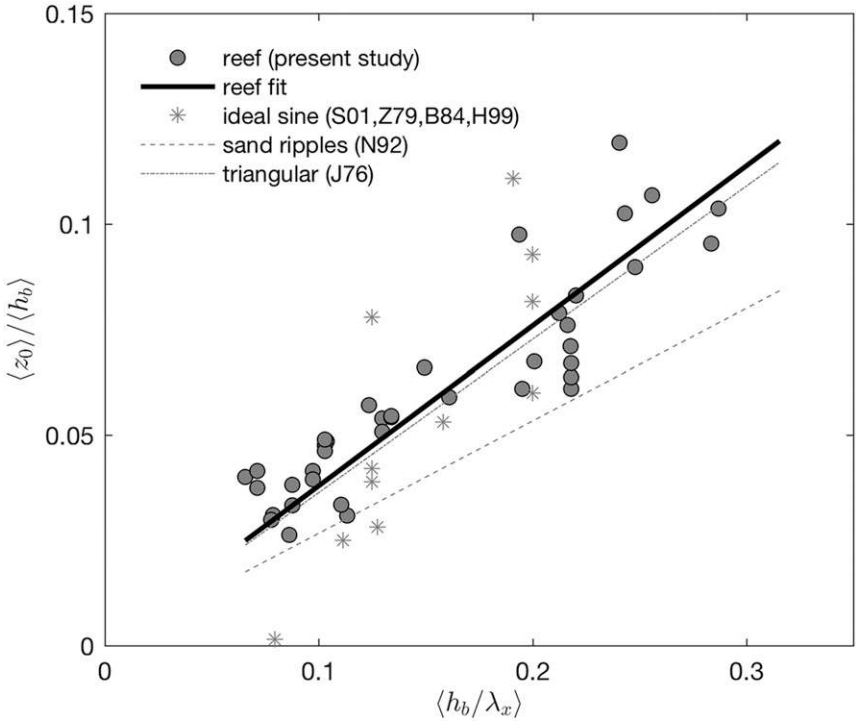

FIG. 11. Hydrodynamic roughness $\langle z_0 \rangle$ from reef model simulations normalized by the roughness length scale $\langle h_b \rangle$ as a function of average streamwise slope $\langle h_b/\lambda_x \rangle$ (circles). Reef parameterization is (18) with slope $a_1 = 0.38$ and $R^2 = 0.79$ (solid). Comparison with results from idealized sinusoidal bathymetry (asterisks) [Salvetti et al. 2001 (S01); Zilker and Hanratty 1979 (Z79); Buckles et al. 1984 (B84); Henn and Sykes 1999 (H99)]; and parameterizations for sand ripples [Nielsen 1992 (N92)] (dashed); and triangular ripples [Jonsson and Carlsen 1976 (J76)] (dotted–dashed).

$O(100)$ m. Based on the momentum balance, we conclude that within the pool the primary terms in the depth-averaged momentum equation are between pressure gradient and bottom stress, a result which is well known in these conditions (Monismith 2007). The pressure gradient develops as a result of breaking waves on the forereef, which are tidally modulated, and drive the unidirectional alongshore flow in the pool. This relatively simple flow in the absence of waves provides the ideal setting to better understand the role of bottom bathymetry of the complex reef in creating hydrodynamic roughness.

Using high-resolution UAV fluid-lensing techniques, we mapped the bottom bathymetry of the pool and used this data to model the reef using the SUNTANS nonhydrostatic hydrodynamic model. The results from the model for bottom drag coefficient $\langle C_{D,B} \rangle$ are in excellent agreement with idealized test cases and generally in good agreement with the field observations, with some scatter likely due to variations in spatial averages from the different methods. The choice of using a RANS model allows for modeling field-scale sections of the reef with moderate computational cost but drastically simplifies the turbulent properties of the flow. Work to extend this analysis using a large-eddy simulation (LES) code could address some of these issues and potentially improve the model results but would require very large computational resources. However, for the purposes of this study, primarily to predict total drag, the selected model appears to be adequate.

The modeled hydrodynamic flows on the reef illustrate the complexity of flows over these surfaces. Wakes form in both the horizontal and vertical, which create imbalances in the pressures, and generally reattach behind the larger reef forms, confirming that many reefs can be characterized as having k–δ-type roughness. These pressure differences lead to form drag $\langle C_{D,p} \rangle$, which is the primary cause of total drag in the model results. Drag due to shear stress $\langle C_{D,\tau} \rangle$ is a minor term except for nearly flat model geometries, a condition that is very rare in reef environments.

For parameterizing the bathymetry and dimensional analysis, we approximate the reef surface as a superposition of wavy sinusoidal bedforms with potentially

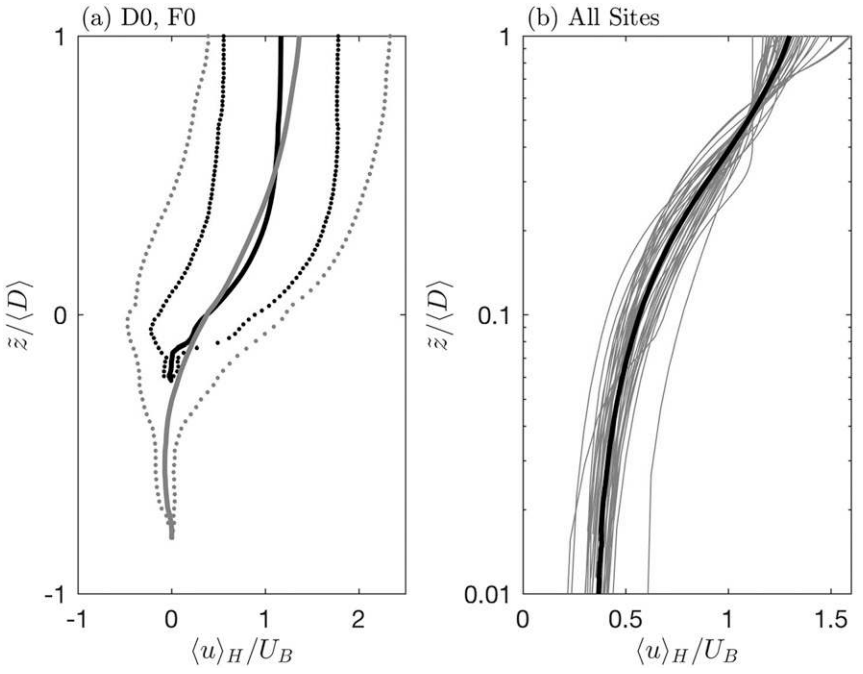

FIG. 12. Vertical profiles of horizontal velocity. (a) Two example sites showing high spatial variability and self-similarity of horizontally averaged flow $\langle u\rangle_H$ above mean depth ($\tilde{z}/\langle D\rangle > 0$) and (b) scaled profiles of all sites showing self-similarity of horizontally averaged profiles above mean depth is logarithmic. For (a) black is site D0, gray is F0, solid is the horizontal average over the model domain $\langle u\rangle_H$, dotted are ±2 standard deviations. For (b) gray lines are horizontal average for each site, black line is average of all sites.

four nondimensional parameters governing the flow. These include a roughness Reynolds number $\mathrm{Re}_h = (U_B\langle h_b\rangle)/\nu$, relative depth $\langle D\rangle/\langle h_b\rangle$, slope in the streamwise direction $\langle h_b/\lambda_x\rangle$, and slope in the spanwise direction $\langle h_b/\lambda_y\rangle$. We approximate these terms by spatially averaging over the model domain, and based on variation of parameters in the model, we conclude that the bulk drag is a function of the relative depth and slope in the streamwise direction only. The direction of flow may be important for certain forms that are not symmetric, the effects of which are not considered in this method.

Roughness on wavy bedforms such as reefs are characterized by *k*–δ-type roughness, which scales with a roughness height and a roughness concentration. Drawing on previous work on sediment bedforms and idealized studies, we propose a parameterization for the bottom roughness scale $\langle z_0\rangle$ [(18)], which is a function of the roughness height based on the spatial rms of the surface $\langle h_b\rangle$, the roughness concentration based on the spatial rms slope $\langle h_b/\lambda_x\rangle$, the coefficient a_1, and the unresolved roughness $\langle z_{0,ur}\rangle$. Combining this equation with an expression for the spatially averaged drag coefficient $\langle C_{D,B}\rangle$ [(19)], a best fit to all model runs, we obtain an $R^2 = 0.79$ and coefficient $a_1 = 0.38$. The results for z_0 compare well to previous studies on idealized sinusoidal and triangular bedforms ($a_1 = 0.36$).

The result in (18) is likely applicable for a range turbulent flows over complex terrains with *k*–δ-type roughness where relative depth $\langle D\rangle/\langle h_b\rangle > 1.1$ and average slope $\langle h_b/\lambda_x\rangle < 0.29$. For very shallow depths $\langle D\rangle/\langle h_b\rangle < 1.1$, the horizontally averaged log-layer approximation likely breaks down and (18) and (19) are no longer valid (Lentz et al. 2017). For very deep cases as $\langle D\rangle/\langle h_b\rangle \to \infty$, the flow becomes a pure boundary layer and (18) is valid, but the depth-averaged approach in (19) is likely not applicable as other forces (e.g., surface, buoyancy, rotation) may become important above the boundary layer.

As $\langle h_b/\lambda_x\rangle$ increases, flow will not reattach between elements, and a larger-scale boundary layer will form dependent only on $\langle h_b\rangle$, characteristic of *k*-type roughness. Thus, the transition from the present study limits $\langle h_b/\lambda_x\rangle = 0.29$ to this new regime will likely occur around $\langle h_b/\lambda_x\rangle = 0.7$ (idealized packed spheres), and further studies into this transition would be of great interest. For very small $\langle h_b/\lambda_x\rangle$, flow may not separate behind roughness elements, leading to a smaller $\langle z_0\rangle$ than predicted by (18). This transition is pronounced for

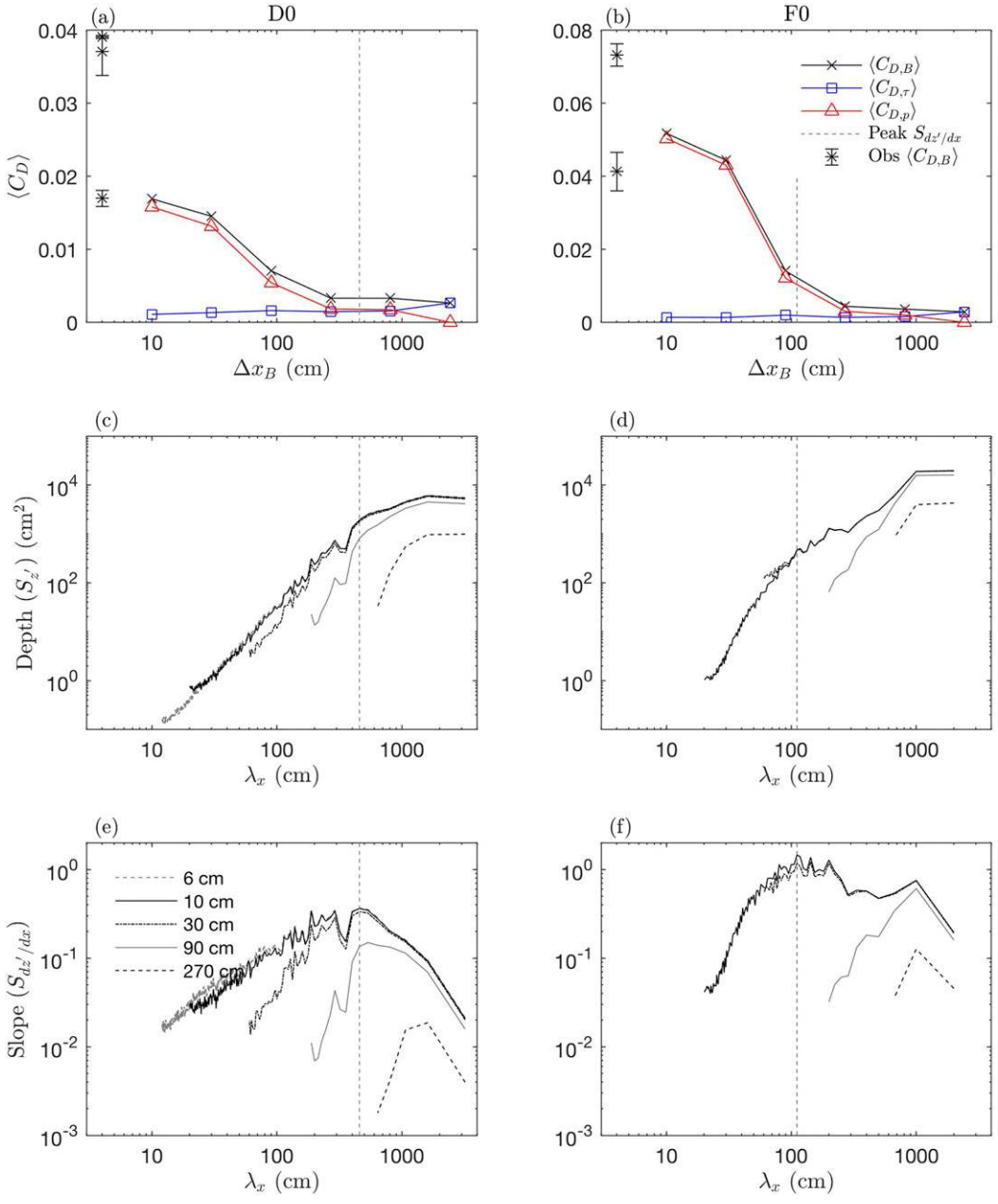

FIG. 13. Computed drag and bathymetry energy spectra at different spatial resolutions at sites (left) D0 and (right) F0. (a),(b) Total $\langle C_{D,B} \rangle$, shear $\langle C_{D,\tau} \rangle$, and form $\langle C_{D,p} \rangle$ drag from the model as a function of bathymetry horizontal grid resolution Δx_B showing $\langle C_{D,B} \rangle$ approaching an asymptotic value indicative of dominant horizontal scale. The observational result for $\langle C_{D,B} \rangle$ is shown for reference with results from different methods as shown in Fig. 6. Spectral energy density of (c),(d) bottom depth surface $S_{z'}$ and (e),(f) bottom slope $S_{dz'/dx}$ as a function of horizontal streamwise wavelength λ_x for different Δx, showing dominant horizontal scale. Vertical dashed line in (a)–(f) shows location of spectral peak in $S_{dz'/dx}$ at the highest resolution a_1. Legend is the same for (a) and (b). Legends are the same for (c)–(f).

idealized sinusoidal bedforms for $\langle h_b/\lambda_x \rangle < 0.1$ but is not observed in the reef model results as irregular forms enhance flow separation. An alternate interpretation for the variation in roughness regimes described above is to instead divide regimes into k- and d-type roughness, which account for roughness density (or solidity) (Jimenez 2004) and should be generally equivalent to varying $\langle h_b/\lambda_x \rangle$.

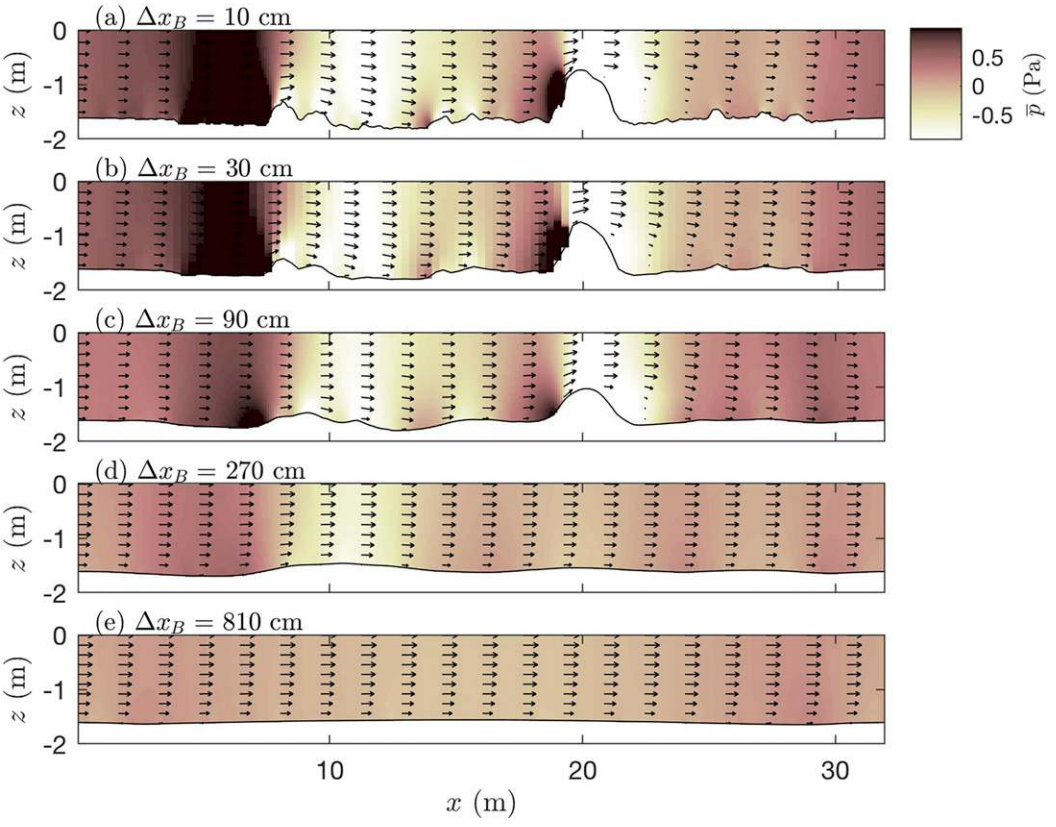

FIG. 14. Dynamic pressure field $\overline{p}$ at site D0 in side plane (x, z) as a function of bathymetry grid resolution Δx_B showing decreasing $\overline{p}$ with decreased resolution, which leads to decreasing form drag. Location is the same as shown in Fig. 4d, and model grid resolution Δx_G is 10 cm. Velocity vector $(\overline{u}, \overline{w})$ scale is 15 cm s^{-1}.

For geometry that is highly resolved, $\langle z_0 \rangle_{ur}$ represents the contribution from shear drag and should tend toward zero with increasing resolution. For coarsely resolved geometry, $\langle z_0 \rangle_{ur}$ represents a parameterization of the form drag, which must be estimated.

While the local velocity profile on the reef is highly variable, the spatially averaged flow is logarithmic above the mean depth and justifies using a log-layer approximation for modeling larger-scale flows. Additionally, while only the slope in the streamwise direction is considered in (18), the spatial averaging does account for some variations in the spanwise direction, since the spatial average is applied in both horizontal directions over some areas. Waveforms that are parallel to flow would yield $\langle h_b/\lambda_x \rangle = 0$ and thus $z_0 = 0$, while flow perpendicular to the same bedforms would give nonzero $\langle h_b/\lambda_x \rangle$ and z_0.

Finally, we investigate which horizontal spatial scales are relevant to creating total drag on the reef. Based on model simulations where we hold the model resolution constant but change the bathymetry resolution using an average of the high-resolution subgrid-scale bathymetry, we find that the drag approaches an asymptote for small scales, implying that a moderate horizontal length scale dominates the drag. This also implies that the very finescale features do not contribute much to the overall pressure field and thus the total drag, the result of the large-scale features creating wakes that isolate the small features from the main flow. This dominant horizontal spatial scale predicted by energy spectra of the slope showed a maximum around the same horizontal length scale of the large roughness features of the reef. A model resolution of O(10–50) grid cells per this dominant spatial scale is required to resolve the flow separation and accurately model the form drag on the reef.

6. Summary

We conducted extensive field observations on a coral reef and developed a nonhydrostatic hydrodynamic model for flows over the complex terrain. We present a simplified method to estimate the hydrodynamic roughness z_0 on a complex surface, with only the rms of

TABLE A1. Field experiment instrumentation and sampling rate for each site.

Instrument	Sample rate	Sites
Sea-Bird 26 (paroscientific digiquartz)	Tide: 10-min avg; waves: 384 burst samples at 2 Hz every 30 min	D-2, K0
Sea-Bird 26+ (paroscientific digiquartz)	Tide: 10-min avg; waves: 1024 burst samples at 2 Hz every 30 min	FR16, CH9
RBR SoloD/1050/Virtuoso	Continuous at 2 Hz (soloD) and 1 Hz (1050, Virtuoso)	A+1, A-1, A-2, A-3, D + 2, D + 1, D0, D-1, D-2, D-3, D-5, FR5, I + 1, I + 2, I-1
RBR DuoBPR (paroscientific digiquartz)	Continuous at 6 Hz	A0, C0, E0, G0, I0
1-MHz Nortek ADP	Profile interval: 5-min, 50-cm bins; waves: 1024 burst samples at 1 Hz every 30 min	FR16, CH9
2-MHz Nortek ADP	Profile interval: 3-min, 15-cm bins; waves: 2048 burst samples at 2 Hz every 30 min	B0, D0, F0, H0, J0
Teledyne vADCP	Continuous at 0.33 Hz, 3-cm bins	B-1, D-4, H-1
Sea-Bird 56 Thermistor	Continuous at 2 Hz	All sites
Sea-Bird 37 CTDO + SBE 63 DO	10 min	D0
Drifters, Garmin GPS	5 s	77 releases, pool 400, High/low/mid tide, 14–22 Mar
Campbell Scientific weather station (wind, temp, Rh, radiometer)	10 min	WS (1.8 km SW of Pool 400)

the depth and streamwise slope as well as a coefficient a_1 required as inputs. Moving forward, the method presented here is likely applicable to other wavy bedforms with k–δ-type roughness. Further work could explore how the coefficient a_1 may vary depending on other flow conditions and geometries and the transition to k-type roughness for high slopes. Additionally, surface waves are common in shallow flows; thus, understanding how oscillatory flows interact with the mean hydrodynamic drag over complex surfaces is a logical next step. Finally, while this method well predicts the average stress to model the large-scale flow, it likely does not well approximate the local bed shear stress, which is often used to model sediment transport and should be investigated further.

Acknowledgments. This work was supported by a grant from the National Science Foundation (OCE-1536502; "Collaborative research: Wave driven flow through a shallow, fringing reef") to SGM, JJA, and CBW. The data from this study are available by request from the corresponding author. Suggestions from two anonymous reviewers, and discussions with Geno Pawlak significantly improved this manuscript. We wish to acknowledge the field team: Annie Adelson, Emma Reid, Benjamin Hefner, Ron Instrella, and Will Roderick. Assistance with modeling was provided by Oliver Fringer, Yun Zhang, Eric Mayer, Kurt Nelson, and Wenhao Chen. This work was conducted under permits from the U.S. Department of the Interior National Park Service, National Park of American Samoa, and the American Samoa Department of Marine and Wildlife Resources.

APPENDIX

Instrumentation, Sampling, and Initial Processing

Pressure, velocity, drifter, conductivity, and temperature measurements were made on the reef, and a weather station was located 1.8 km to the southwest (Table A1). Monitoring stations with larger instruments were attached to polyethylene plates and secured to the reef in areas of dead coral or sand. Monitoring stations with only small sensors were secured directly to dead corals or rubble.

The measured pressure p is filtered to obtain η_{hyd}, the free surface deviation due to hydrodynamic processes; see the supplemental material. The net offset $\eta_0(x)$ at each site between h and MSL is determined from (3):

$$\Delta\eta_{\mathrm{hyd}} + \Delta\eta_0 = \frac{L}{g}(-\mathrm{US} - \mathrm{NL} - \mathrm{RSG} - \mathrm{BT} + \mathrm{ST}), \tag{A1}$$

where $\Delta\eta_{\mathrm{hyd}} = \eta_{\mathrm{hyd}}(x_2) - \eta_{\mathrm{hyd}}(x_1)$, and $\Delta\eta_0$ is the intercept in the least squares sense for the smallest 10% of the sum of the RHS; that is, as forcing approaches zero, water slope should be flat (Monismith et al. 2013; Lentz et al. 2016). The terms in parentheses in (A1) are described in section 3b. The mean surface stress $\overline{\boldsymbol{\tau}_s}$ is approximated by a quadratic drag law, $\overline{\boldsymbol{\tau}_s} = \rho_a C_{Da} \mathbf{U}_{10} |\mathbf{U}_{10}|$, where ρ_a is air density, C_{Da} is the wind drag coefficient, and $\mathbf{U}_{10}$ is wind velocity (Smith 1988). At the forereef sites, $\eta_0 = 0$, and η_0 at the first reef site onshore of the surfzone (K0) is estimated from the wave energy flux

using the method of Vetter et al. 2010. Wave analysis is conducted using standard spectral methods (Dean and Dalrymple 1991); see the supplemental material.

An alternate method of computing the mean bottom stress $\overline{\boldsymbol{\tau}_b}$ is computed from the turbulent Reynolds stress, which is assumed constant within the inertial sublayer (Reidenbach et al. 2006), $\overline{\boldsymbol{\tau}_b} = -\rho\overline{\mathbf{u}'w'}$, using the measured turbulent velocities $\mathbf{u}'$ from the ADVs and removing wave effects (Benilov and Filyushkin 1970). Combining with (1) gives

$$C_D = \frac{-\overline{\mathbf{u}'w'}}{U|\mathbf{U}|}. \tag{A2}$$

REFERENCES

Bearman, P. W., 1971: An investigation of the forces on flat plates normal to a turbulent flow. *J. Fluid Mech.*, **46**, 177–198, https://doi.org/10.1017/S0022112071000478.

Benilov, A. Y., and B. N. Filyushkin, 1970: Application of methods of linear filtration to an analysis of fluctuations in the surface layer of the sea. *Izv. Akad. Nauk SSSR, Fiz. Atmos. Okeana*, **6**, 810–819.

Buckles, J., T. J. Hanratty, and R. J. Adrian, 1984: Turbulent flow over large-amplitude wavy surfaces. *J. Fluid Mech.*, **140**, 27–44, https://doi.org/10.1017/S0022112084000495.

Chirayath, V., 2016: Fluid lensing and applications to remote sensing of aquatic environments. Ph.D. dissertation, Stanford University, 177 pp., https://purl.stanford.edu/kw062mg5196.

——, and S. A. Earle, 2016: Drones that see through waves—Preliminary results from airborne fluid lensing for centimetre-scale aquatic conservation. *Aquat. Conserv.*, **26**, 237–250, https://doi.org/10.1002/aqc.2654.

Dean, R. G., and R. A. Dalrymple, 1991: *Water Wave Mechanics for Engineers and Scientists*. Advanced Series on Ocean Engineering, Vol. 2, World Scientific, 353 pp.

Falter, J. L., M. J. Atkinson, and M. A. Merrifield, 2004: Mass-transfer limitation of nutrient uptake by a wave-dominated reef flat community. *Limnol. Oceanogr.*, **49**, 1820–1831, https://doi.org/10.4319/lo.2004.49.5.1820.

Feddersen, F., E. L. Gallagher, R. T. Guza, and S. Elgar, 2003: The drag coefficient, bottom roughness, and wave-breaking in the nearshore. *Coastal Eng.*, **48**, 189–195, https://doi.org/10.1016/S0378-3839(03)00026-7.

Fringer, O. B., M. Gerritsen, and R. L. Street, 2006: An unstructured-grid, finite-volume, nonhydrostatic, parallel coastal ocean simulator. *Ocean Modell.*, **14**, 139–173, https://doi.org/10.1016/j.ocemod.2006.03.006.

Gong, W., P. Taylor, and A. Dörnbrack, 1996: Turbulent boundary-layer flow over fixed aerodynamically rough two-dimensional sinusoidal waves. *J. Fluid Mech.*, **312**, 1–37, https://doi.org/10.1017/S0022112096001905.

Grant, W. D., and O. S. Madsen, 1979: Combined wave and current interaction with a rough bottom. *J. Geophys. Res.*, **84**, 1797–1808, https://doi.org/10.1029/JC084iC04p01797.

——, and ——, 1982: Movable bed roughness in unsteady oscillatory flow. *J. Geophys. Res.*, **87**, 469–481, https://doi.org/10.1029/JC087iC01p00469.

Hearn, C. J., 1999: Wave-breaking hydrodynamics within coral reef systems and the effect of changing relative sea level. *J. Geophys. Res.*, **104**, 30 007–30 019, https://doi.org/10.1029/1999JC900262.

——, 2011a: Hydrodynamics of coral reef systems. *Encyclopedia of Modern Coral Reefs: Structure, Form and Process*, D. Hopley, Ed., Springer, 563–573.

——, 2011b: Perspectives in coral reef hydrodynamics. *Coral Reefs*, **30**, 1–9, https://doi.org/10.1007/s00338-011-0752-4.

Hench, J. L., and J. H. Rosman, 2013: Observations of spatial flow patterns at the coral colony scale on a shallow reef flat. *J. Geophys. Res. Oceans*, **118**, 1142–1156, https://doi.org/10.1002/jgrc.20105.

Henn, D. S., and R. I. Sykes, 1999: Large-eddy simulation of flow over wavy surfaces. *J. Fluid Mech.*, **383**, 75–112, https://doi.org/10.1017/S0022112098003723.

Jaramillo, S., and G. Pawlak, 2011: AUV-based bed roughness mapping over a tropical reef. *Coral Reefs*, **30**, 11–23, https://doi.org/10.1007/s00338-011-0731-9.

Jimenez, J., 2004: Turbulent flows over rough walls. *Annu. Rev. Fluid Mech.*, **36**, 173–196, https://doi.org/10.1146/annurev.fluid.36.050802.122103.

Jonsson, I. G., and N. A. Carlsen, 1976: Experimental and theoretical investigations in an oscillatory turbulent boundary layer. *J. Hydraul. Res.*, **14**, 45–60, https://doi.org/10.1080/00221687609499687.

Koweek, D. A., R. B. Dunbar, S. G. Monismith, D. A. Mucciarone, C. B. Woodson, and L. Samuel, 2015: High-resolution physical and biogeochemical variability from a shallow back reef on Ofu, American Samoa: An end-member perspective. *Coral Reefs*, **34**, 979–991, https://doi.org/10.1007/s00338-015-1308-9.

Kundu, P. K., and I. M. Cohen, 2008: *Fluid Mechanics.* 4th ed. Academic Press, 872 pp.

Lentz, S. J., J. H. Churchill, K. A. Davis, J. T. Farrar, J. Pineda, and V. Starczak, 2016: The characteristics and dynamics of wave-driven flow across a platform coral reef in the Red Sea. *J. Geophys. Res. Oceans*, **121**, 1360–1376, https://doi.org/10.1002/2015JC011141.

——, K. A. Davis, J. H. Churchill, and T. M. DeCarlo, 2017: Coral reef drag coefficients—Water depth dependence. *J. Phys. Oceanogr.*, **47**, 1061–1075, https://doi.org/10.1175/JPO-D-16-0248.1.

Lettau, H., 1969: Note on aerodynamic roughness-parameter estimation on the basis of roughness-element description. *J. Appl. Meteor.*, **8**, 828–832, https://doi.org/10.1175/1520-0450(1969)008<0828:NOARPE>2.0.CO;2.

Lowe, R. J., J. R. Koseff, and S. G. Monismith, 2005: Oscillatory flow through submerged canopies: 1. Velocity structure. *J. Geophys. Res.*, **110**, C10016, https://doi.org/10.1029/2004JC002788.

Lübcke, H., S. Schmidt, T. Rung, and F. Thiele, 2001: Comparison of LES and RANS in bluff-body flows. *J. Wind Eng. Ind. Aerodyn.*, **89**, 1471–1485, https://doi.org/10.1016/S0167-6105(01)00134-9.

McDonald, C. B., J. R. Koseff, and S. G. Monismith, 2006: Effects of the depth to coral height ratio on drag coefficients for unidirectional flow over coral. *Limnol. Oceanogr.*, **51**, 1294–1301, https://doi.org/10.4319/lo.2006.51.3.1294.

Mei, C., M. Stiassnie, and D. Yue, 2005: *Theory and Applications of Ocean Surface Waves*. Advanced Series on Ocean Engineering, Vol. 23, World Scientific, 1071 pp.

Monismith, S. G., 2007: Hydrodynamics of coral reefs. *Annu. Rev. Fluid Mech.*, **39**, 37–55, https://doi.org/10.1146/annurev.fluid.38.050304.092125.

——, L. M. M. Herdman, S. Ahmerkamp, and J. L. Hench, 2013: Wave transformation and wave-driven flow across a steep

coral reef. *J. Phys. Oceanogr.*, **43**, 1356–1379, https://doi.org/10.1175/JPO-D-12-0164.1.

Nelson, K. S., and O. B. Fringer, 2017: Reducing spin-up time for simulations of turbulent channel flow. *Phys. Fluids*, **29**, 105101, https://doi.org/10.1063/1.4993489.

Nielsen, P., 1992: *Coastal Bottom Boundary Layers and Sediment Transport.* World Scientific, 323 pp.

Nikuradse, J., 1933: Strömungsgesetze in Rauhen Rohren. Verein Deutscher Ingenieure Forschungsheft 361, 22 pp.

Nunes, V., and G. Pawlak, 2008: Observations of bed roughness of a coral reef. *J. Coastal Res.*, **24**, 39–50, https://doi.org/10.2112/05-0616.1.

Perry, A., W. H. Schoflield, and P. N. Joubbert, 1969: Rough wall turbulent boundary layers. *J. Fluid Mech.*, **37**, 383–413, https://doi.org/10.1017/S0022112069000619.

Reidenbach, M. A., S. G. Monismith, J. R. Koseff, G. Yahel, and A. Genin, 2006: Boundary layer turbulence and flow structure over a fringing coral reef. *Limnol. Oceanogr.*, **51**, 1956–1968, https://doi.org/10.4319/lo.2006.51.5.1956.

Rodi, W., 1997: Comparison of LES and RANS calculations of the flow around bluff bodies. *J. Wind Eng. Ind. Aerodyn.*, **69–71**, 55–75, https://doi.org/10.1016/S0167-6105(97)00147-5.

Rogers, J. S., S. G. Monismith, R. B. Dunbar, and D. Koweek, 2015: Field observations of wave-driven circulation over spur and groove formations on a coral reef. *J. Geophys. Res. Oceans*, **120**, 145–160, https://doi.org/10.1002/2014JC010464.

——, ——, D. A. Koweek, W. I. Torres, and R. B. Dunbar, 2016: Thermodynamics and hydrodynamics in an atoll reef system and their influence on coral cover. *Limnol. Oceanogr.*, **61**, 2191–2206, https://doi.org/10.1002/lno.10365.

——, ——, O. B. Fringer, D. A. Koweek, and R. B. Dunbar, 2017: A coupled wave-hydrodynamic model of an atoll with high friction: Mechanisms for flow, connectivity, and ecological implications. *Ocean Modell.*, **110**, 66–82, https://doi.org/10.1016/j.ocemod.2016.12.012.

Roshko, A., 1961: Experiments on the flow past a circular cylinder at very high Reynolds number. *J. Fluid Mech.*, **10**, 345–356, https://doi.org/10.1017/S0022112061000950.

Rosman, J. H., and J. L. Hench, 2011: A framework for understanding drag parameterizations for coral reefs. *J. Geophys. Res.*, **116**, C08025, https://doi.org/10.1029/2010JC006892.

Salvetti, M. V., R. Damiani, and F. Beux, 2001: Three-dimensional coarse large-eddy simulations of the flow above two-dimensional sinusoidal waves. *Int. J. Numer. Methods Fluids*, **35**, 617–642, https://doi.org/10.1002/1097-0363(20010330)35:6<617::AID-FLD104>3.0.CO;2-M.

Schlichting, H., 1979: *Boundary-Layer Theory*. 7th ed. McGraw-Hill, 817 pp.

Smith, S. D., 1988: Coefficients for sea surface wind stress, heat flux, and wind profiles as a function of wind speed and temperature. *J. Geophys. Res.*, **93**, 15 467–15 472, https://doi.org/10.1029/JC093iC12p15467.

Suosaari, E. P., and Coauthors, 2016: New multi-scale perspectives on the stromatolites of Shark Bay, Western Australia. *Nat. Sci. Rep.*, **6**, 20557, https://doi.org/10.1038/srep20557.

Swart, D. H., 1977: Predictive equations regarding coastal transports. *Coastal Eng.*, **104**, 1149–1158, https://doi.org/10.1061/9780872620834.066.

Symonds, G., K. P. Black, and I. R. Young, 1995: Wave-driven flow over shallow reefs. *J. Geophys. Res.*, **100**, 2639–2648, https://doi.org/10.1029/94JC02736.

Thomas, F. I. M., and M. J. Atkinson, 1997: Ammonium uptake by coral reefs: Effects of water velocity and surface roughness on mass transfer. *Limnol. Oceanogr.*, **42**, 81–88, https://doi.org/10.4319/lo.1997.42.1.0081.

Vetter, O., J. M. Becker, M. A. Merrifield, C. Pequignet, J. Aucan, S. J. Boc, and C. E. Pollock, 2010: Wave setup over a Pacific island fringing reef. *J. Geophys. Res.*, **115**, C12066, https://doi.org/10.1029/2010JC006455.

Warner, J. C., C. R. Sherwood, H. G. Arango, and R. P. Signell, 2005: Performance of four turbulence closure models implemented using a generic length scale method. *Ocean Modell.*, **8**, 81–113, https://doi.org/10.1016/j.ocemod.2003.12.003.

Wooding, R. A., E. F. Bradley, and J. K. Marshall, 1973: Drag due to regular arrays of roughness elements of varying geometry. *Bound.-Layer Meteor.*, **5**, 285–308, https://doi.org/10.1007/BF00155238.

Zilker, D. P., and T. J. Hanratty, 1979: Influence of the amplitude of a solid wavy wall on a turbulent flow. Part 2. Separated flows. *J. Fluid Mech.*, **90**, 257–271, https://doi.org/10.1017/S0022112079002196.